# Shifting demand: Reduction in necessary storage capacity through tracking of renewable energy generation

Dylan Wald [a,b,*], Kathryn Johnson [a,b], Jennifer King [a], Joshua Comden [a], Christopher J. Bay [a], Rohit Chintala [a], Sanjana Vijayshankar [a], Deepthi Vaidhynathan [a]

[a] *National Renewable Energy Laboratory, 15013 Denver W Pkwy, Golden, CO 80401, USA*
[b] *Colorado School of Mines, 1500 Illinois St., Golden, CO 80401, USA*

ABSTRACT

Renewable energy (RE) generation systems are rapidly being deployed on the grid. In parallel, electrified devices are quickly being added to the grid, introducing additional electric loads and increased load flexibility. While increased deployment of RE generation contributes to decarbonization of the grid, it is inherently variable and unpredictable, introducing uncertainty and potential instability in the grid. One way to mitigate this problem is to deploy utility-scale storage. However, in many cases the deployment of utility-scale battery storage systems remain unfeasible due to their cost. Instead, utilizing the increased amounts of data and flexibility from electrified devices on the grid, advanced control can be applied to shift the demand to match RE generation, significantly reducing the capacity of required utility-scale battery storage. This work introduces the novel forecast-aided predictive control (FAPC) algorithm to optimize this load shifting in the presence of forecasts. Extending upon an existing coordinated control framework, the FAPC algorithm introduces a new electric vehicle charging control algorithm that has the capability to incorporate forecasted information in its control loop. This enables FAPC to better track a realistic RE generation signal in a fully correlated simulation environment. Results show that FAPC effectively shifts demand to track a RE generation signal under different weather and operating conditions. It is found that FAPC significantly reduces the required capacity of the battery storage system compared to a baseline control case.

## 1. Introduction

Aggressive clean energy incentives and goals have recently become more widespread across the United States and the world. As a result, the penetration of renewable energy (RE) devices across the United States and the world continue to break records. According to the U.S. Energy Information Administration (EIA), 2020 was the first year RE and nuclear combined produced more energy than coal. That being said, the dominant technologies in RE generation are wind and solar [1]. While this indicates that the grid is quickly moving toward decarbonization, it's available generation is becoming more intermittent and unreliable. Because wind and solar generation both depend on stochastic weather conditions, these RE-generated energy sources are nondispatchable. In a system dependent on this intermittent generation, peak demand may occur at different times than peak generation, leading to demand not matching generation. This is a major issue in the eyes of the power system (grid), potentially leading to dangerous frequency and voltage instabilities [2].

*One solution* to the generation-demand mismatch caused by intermittent RE generation is to deploy utility-scale battery energy storage systems (BESS) [3]. In times when RE generation exceeds demand, excess energy can be stored. This energy can then be dispatched in times when demand exceeds generation. This storage and release of energy is nearly instantaneous, providing highly responsive ancillary services to the grid [4]. While BESSs are able to provide ancillary services and improve dispatchability, current BESS technologies have several challenges. These challenges include, but are not limited to, an inadequate safety validation, degradation of the BESS, and most crucial, cost of BESSs [3,4]. Due to these challenges, it may be beneficial to limit the total BESS capacity required for deployment.

*Another solution* to the generation-demand mismatch is to shift the demand. In addition to using RE generation sources, decarbonizing the grid requires electrification of fuel-based energy consumers. For instance, electric vehicles (EVs) and hybrid EVs accounted for 11% of all light-duty vehicle sales in the United States at the end of 2021 and are expected to increase to 58% by 2040 [6,5]. In another example, about 40% of a building's energy consumption comes through its heating, ventilation and air-conditioning (HVAC) system, and nearly 40% of U.S. buildings are now heated electrically [7]. As of 2021, commercial buildings and transportation accounted for nearly 50% of total U.S. en-

## Nomenclature

*General*

| | |
|---|---|
| $(\cdot)_m$ | Subscript denoting LC-DMPC subsystem index |
| $(\cdot)_b$ | Subscript denoting building subsystem |
| $(\cdot)_{cs}$ | Subscript denoting charging station subsystem |
| $(\cdot)_{ga}$ | Subscript denoting grid aggregator subsystem |
| $\alpha$ | Renewable energy generation scaling factor |
| $\dot{Q}_{GHI}$ | Global horizontal irradiance (GHI) |
| $E_{B,DA}$ | Energy consumed in the building load forecast |
| $E_{EV,DA}$ | Energy consumed in the EVDAP |
| $E_{RE,DA}$ | Energy consumed in the renewable energy generation forecast |
| $k$ | LC-DMPC communication iteration |
| $N$ | Total number of immediate neighboring subsystems to the grid aggregator subsystem |
| $P_{B,DA}$ | Building forecast |
| $P_b$ | Current building load |
| $P_{RE,DA}$ | Renewable energy generation forecast |
| $P_{ref}$ | Bulk power reference signal from the grid |
| $P_{set}$ | Power set point from the grid aggregator |
| $T$ | Total time duration of simulation |
| $t$ | Discrete time |

*Building Subsystem*

| | |
|---|---|
| $(\cdot)_d$ | Subscript denoting external disturbances |
| $(\cdot)_u$ | Subscript denoting control inputs |
| $(\cdot)_v$ | Subscript denoting upstream disturbances |
| $\bar{U}$ | Upper bound on input vector |
| $\dot{m}_s$ | Mass flow rate of the building HVAC system |
| $\dot{Q}_{HVAC}$ | The heat flow from the building HVAC system |
| $\dot{Q}_{solar}$ | Solar heat flow into the building |
| $\Lambda$ | Diagonal weight matrix for control action energy minimization |
| $\Psi$ | Set of received sensitivity vectors across prediction horizon |
| $\underline{Q}_{HVAC}, \bar{Q}_{HVAC}$ | Lower and upper bounds on the HVAC heat flow in the building forecast algorithm |
| $\underline{T}_b, \bar{T}_b$ | Lower and upper building internal temperature comfort bounds |
| $\underline{U}$ | Lower bound on input vector |
| $\underline{u}_1, \bar{u}_1$ | Lower and upper bounds on the first control input building forecast algorithm |
| $\underline{u}_2, \bar{u}_2$ | Lower and upper bounds on the second control input building forecast algorithm |
| $\{A, B, C, D\}$ | System state, input, output, and disturbance matrices |
| $d$ | External disturbance vector |
| $f_b(\cdot)$ | Function encompassing the building thermodynamic model |
| $J$ | Objective function |
| $Q$ | Diagonal weight matrix for quadratic error cost |
| $R, r$ | Reference vector, set of reference vectors across prediction horizon |
| $S$ | Weight matrix for quadratic control input cost |
| $T_b$ | Building internal temperature |
| $T_{ref}$ | The desired building internal temperature (temperature reference) |
| $T_{sa}$ | Supply air temperature from the building HVAC system |
| $u, U$ | Control input vector, set of control input vectors across prediction horizon |

| | |
|---|---|
| $v, V$ | Input disturbance from upstream neighbors, set of input disturbances from upstream neighbors across prediction horizon |
| $x_0$ | Initial state vector |
| $y, Y$ | Output vector, set output vectors across prediction horizon |
| $z, Z$ | Output disturbance sent to downstream subsystems, set of output disturbances sent to downstream subsystems across prediction horizon |

*Charging Station Subsystem*

| | |
|---|---|
| $(\cdot)^a$ | Denotes arrival index of a variable |
| $(\cdot)^d$ | Denotes departure index of a variable |
| $\bar{p}$ | Maximum charging rate for all EVs |
| $\delta$ | Amount to shift the initial EVDAP plan to ensure feasibility |
| $\Delta_T$ | Length of time step (one minute) |
| $\mathcal{J}$ | Set of EVs at the charging station |
| $\omega_1, \omega_2, \omega_3, \omega_4, \omega_5$ | Weight on EVCS objective components 1–5 |
| $\zeta_{DA}$ | The real-time scaling factor for the EVDAP |
| $E_{EV,U}^t$ | Total energy from time 0 to $t$ used by specified EVs at EVCS |
| $j$ | Individual EV index |
| $p$ | EV charging rate |
| $P^{t,k}$ | Aggregate charging rate at time $t$ and communication iteration $k$ |
| $P_{diff}$ | Difference between $P_{rt}$ and $P_{EV,DA}$ |
| $P_{EV,DA}$ | EVDAP |
| $P_{rt-track}^{t,k}$ | Augmented reference signal from building subsystem at time $t$ and communication iteration $k$ |
| $P_{rt}$ | Aggregate day-ahead profile using the real-time algorithm |
| $SoC$ | State of charge |

*Acronyms*

| | |
|---|---|
| $3R2C$ | 3-resistor 2-capacitor |
| $ADMM$ | alternating direction method of multipliers |
| $AHU$ | air handling unit |
| $BEMS$ | building energy management system |
| $BESS$ | battery energy storage system |
| $EV$ | electric vehicle |
| $EVCS$ | electric vehicle charging station |
| $EVDAP$ | electric vehicle day-ahead plan |
| $FAPC$ | forecast-aided predictive control |
| $FLORIS$ | FLOw Redirection and Induction in Steady state |
| $GA$ | grid aggregator |
| $HVAC$ | heating, ventilating and air conditioning |
| $LC-DMPC$ | limited communication distributed model predictive control |
| $MPC$ | Model Predictive Control |
| $NREL$ | National Renewable Energy Laboratory |
| $NSRDB$ | National Solar Radiation Database |
| $RE$ | renewable energy |

ergy consumption [8]. As devices on the grid continue to electrify, EVs and buildings will represent a large fraction of total energy consumption on the grid. Therefore, research focused on shifting the demand of EVs and buildings is imperative. The advanced control proposed in this work provides a framework to do just that.

### 1.1. State of the art: Single application methods

Both EV charging and building control to achieve various goals have been topics of investigation for some time. Due to their rapidly growing penetration and impact on the grid, many different strategies for EV

charging control have been investigated. These strategies include but are not limited to load shifting [9–12], demand-side management [13,14], and reinforcement learning [15]. Apart from EV charging control, works such as in [16–20], and [21] investigate the complex problem of forecasting EV charging events [16–21] dive deeper into the social aspects of EV event forecasting, the data that should be used, and their methods (probability-based models to complex machine learning methods). However, none discuss or quantify their direct effect on or contribution to the power system, a research gap that this work addresses. Last, the work in [22] combines EV charging control and forecasting by numerically evaluating two different optimization and forecasting approaches to minimize cost in a day-ahead electricity market.

In buildings, model predictive control (MPC) has proven to be a successful method to control building HVAC systems. In building HVAC control, MPC can incorporate various objective functions and constraints such as in [23–26]. Distributed model predictive control (DMPC) allows the possibility of parallel control of more complex building models, multi zone buildings, and multibuilding systems. DMPC has provided significant positive impacts in addressing the complexity and scalability issues of building control. Some examples of DMPC for buildings can be seen in [27–29]. More recently, advances in learning-based and learning-enhanced control for buildings have also been gaining traction, as in works [30] and [31].

*1.2. State of the art: Multi-application methods*

In addition to individual building and EV charging control, studies have also investigated the coordinated control between buildings and EVs to benefit the grid. In this section, we first highlight two works that are most similar to the work introduced in this paper. Then, some other papers exploring similar concepts are summarized.

The work in [32] introduces a Dantzig-Wolfe decomposition algorithm (DWDA) that allows a building and EV charging station to coordinate their power consumption via coupled constraints. The idea is to minimize the cost of energy (COE) due to an energy tariff. This work models building thermodynamics and models the $SoC$ and degradation of EV batteries. This work also uses perfect forecasts to estimate EV events and disturbances to the building. However, this work presents a scheduling algorithm, thus the DWDA solves one-shot optimization problem across an entire control horizon. A dynamic programming type of problem may break down with non-perfect forecasts and modelling error, something that an online, MPC-based algorithm (such as in this work) can better handle. Also, work in [32] is price-driven and does not focus on grid stability.

Like the work in this paper, [33] presents a DMPC method in which heterogeneous devices solve a local MPC problem as well as coordinate to satisfy a global constraint. The DMPC algorithm is demonstrated using buildings, EV charging stations, and energy storage however has the capability to include different devices. The buildings are modeled using thermodynamics and the EV and storage are modeled by monitoring their respective $SoC$'s. Forecasts with uncertainty, a critical component not considered in this paper, are used to compute PV generation which is used to determine a global power flow constraint. However their DMPC algorithm requires a centralized location (a "blackboard") for subsystems to publish and receive information, something not required in this paper. The authors of [33] acknowledge that this "blackboard" introduces a single point of failure, a major drawback of their algorithm.

Other works have also explored the coordinated building – EV charging problem. The work in [34] introduces a two-stage stochastic mixed integer program to minimize COE usage between group of buildings and EVs. The work in [35] introduces a two layer optimization problem that uses a genetic algorithm to determine optimal EV charge rates and a nonlinear program to find optimal sharing of onsite RE and energy storage with respect to EV demand, reducing COE to buildings. The work in [36] develops a stochastic simulation-based policy improvement method using Markov decision processes. The goal is to explore how stochastic rooftop wind energy mixed with flexible onsite EV charging can maximize profit of the buildings. The work in [37] introduces a energy management system as a mixed integer linear program (MILP) to coordinate between different distributed energy resources to minimize total COE. The work in [38] presents a two-step, transactive algorithm where a building energy management system (BEMS) first computes a pre-schedule to maximize its profit subject to uncertain generation and charging events. The BEMS then solves an MPC problem in real-time to determine optimal EV charge rates such that the pre-schedule is tracked. The works in [39] and [40] are very similar in that they introduce a method to reduce the COE to a BEMS aggregator. While [39] accounts for the COE to each EV owner, [40] accounts for other electrical equipment costs and EV owner preferences (amount of adherence to the BEMS policy) while tracking a pre-computed load signal. Last, the work in [41] introduces a two stage stochastic optimization model to determine energy bids for the day ahead (DA) and reserve markets accounting for uncertain real-time demand and generation outcomes.

The aforementioned works [34–41] each include *unique contributions* to the building – EV coordination problem, but exhibit *research gaps* addressed in this paper. [34–37,41] solve a one-shot scheduling problem with full communication. In this paper, an online limited communication problem is solved. While all references [34–40] include a coordination scheme, the building to EV focus is lopsided. None model building thermodynamics, focusing more on the EV charging flexibility. This work models and controls all subsystems equally. Additionally, a subset do not use forecasts [36,39] or do not incorporate RE generation [34,39,40]. Both the use of forecasts and RE generation are an integral part of this paper. An exception is [41], which computes a DA market plan using forecasting algorithms and incorporates uncertain PV generation. However, evidence of a coordination method in [41] is unclear. Last, these works only concern demand shifting to minimize COE. This paper concerns shifting demand to match RE generation to increase grid reliability.

*1.3. System overview*

Fig. 1 displays the overall framework introduced in this paper. The FAPC algorithm (black dashed block at the top of Fig. 1) includes three subsystems: EV charging station (EVCS), building, and grid aggregator. Each subsystem includes a local controller (orange, blue, and red blocks, respectively) that uses real-time data (charging events, building occupancy, RE generation, and weather blocks) to shift demand. The EV charging controller incorporates information from the Forecast Component (bottom left block in Fig. 1). The Forecast Component uses forecasted EV charging events (orange circle), building occupancy (blue circle), and RE generation (red circle) to compute an optimal trajectory for the EV charging controller to follow. Once demand is shifted by the FAPC algorithm, the remaining tracking error is sent to the Storage Component (bottom right block in Fig. 1). The Storage Component decides the amount of power to inject or withdraw from the system to enable perfect tracking, all while monitoring the BESS $SoC$.

*1.4. Contributions*

To motivate the work in this paper, we highlight the Network Lasso ADMM - limited communication - DMPC (NALD) algorithm introduced in [42]. The NALD algorithm allows the coordination between locally controlled subsystems, namely a building and a cluster of charging stations, to track a reference signal from the grid. The success of the NALD algorithm for a *specific scenario* was proven in [42] and was updated in [43] to handle more *general scenarios* using *arbitrary* reference signals.

In this work, we introduce the forecast-aided predictive control (FAPC) algorithm (dashed black box in Fig. 1). FAPC is an extension of the NALD algorithm discussed in [42] and [43]. Specific contributions of this work include:
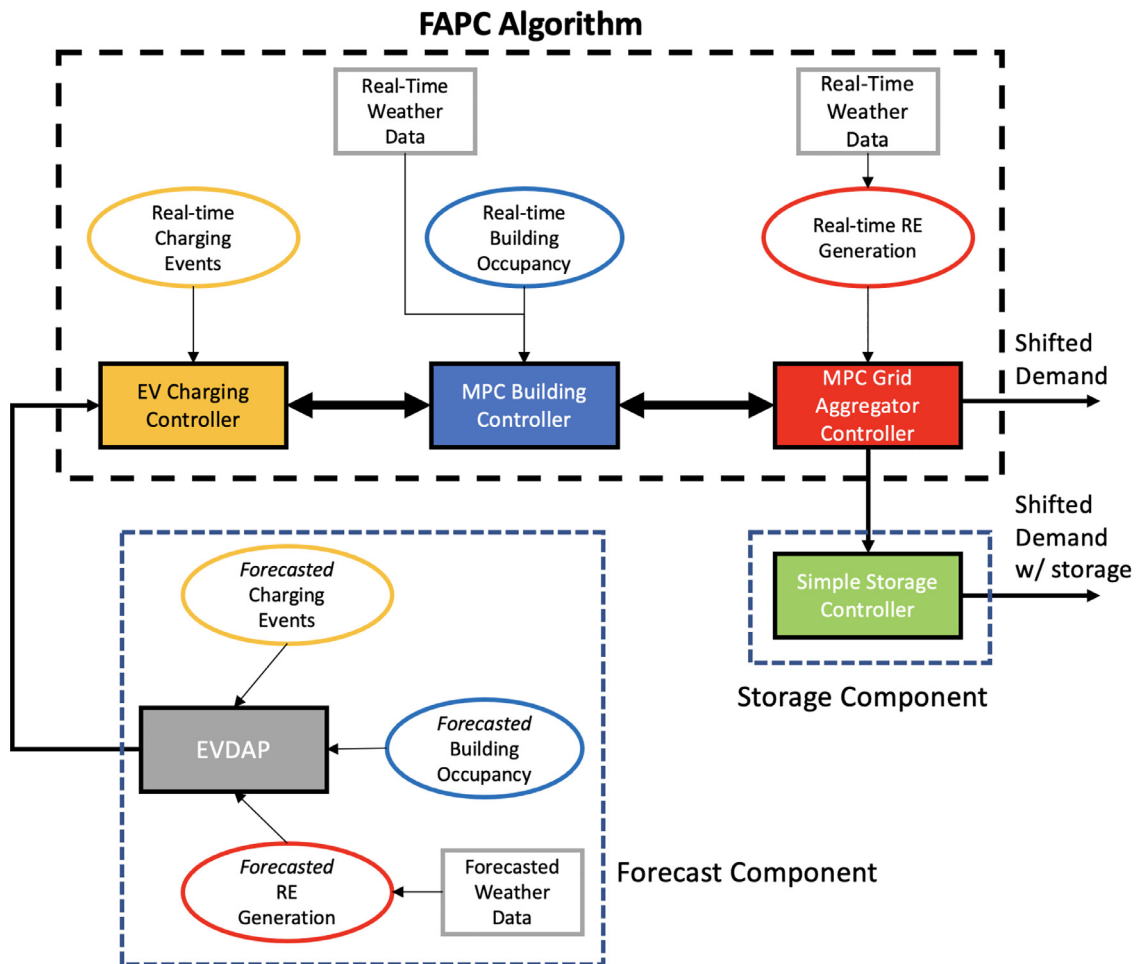
**Fig. 1.** Flowchart describing the novel framework implemented in this paper. This consists of a Forecast Component (bottom-left block), the novel FAPC algorithm (top block), and the Storage Component (bottom-right block). The Forecast Component is first computed offline, then used in the novel, real-time FAPC algorithm. The Storage Component then determines the amount of storage power the utility-scale BESS dispatches into the system to perfectly track the RE generation.

- **Updated EV charging control algorithm**
  This paper replaces the Network Lasso - ADMM charging station control algorithm in the NALD algorithm with a simplified centralized control algorithm. The new EV charging control algorithm is less complex, more realistically represents a charging station connected to a building, and has the ability to use forecasts (see orange EV Charging Controller block in Fig. 1).

- **Forecast component**
  A benefit of the new charging station control algorithm is that it has the ability to *utilize* a day-ahead charging plan (Forecast Component in Fig. 1), built from neighboring subsystem forecasts, to improve the load shifting abilities of both the EVCS and the system as a whole. The Forecast Component uses perfect forecasts, creating an upper bound to the optimal EV charging plan.

- **Tracking realistic reference signal**
  This paper evaluates the performance of FAPC by tracking a *realistic* RE generation signal as opposed to an *arbitrary* reference signal like in [42] and [43]. The RE generation signal is constructed from the same weather data that is used as disturbances to subsystems in the system (a fully correlated simulation environment). This enables the opportunity to analyze FAPC performance in a *realistic* scenario with *intermittent* generation, a challenging but realistic phenomenon.

- **Robustness analyses**
  This paper analyzes the robustness of FAPC to different *weather and RE generation conditions*, different *occupancy schedules*, and different *day-ahead plan accuracy*.

- **Storage component**
  In this paper, it is assumed that *perfect tracking* of the RE generation will ensure grid stability (demand equals generation). For this to be possible, we include a utility-scale BESS to account for the FAPC tracking error. The performance of FAPC is quantified as the size of the required BESS needed such that the demand perfectly tracks the RE generation. The amount of BESS power to inject or remove, in addition to the state ($SoC$) of the BESS, is determined in the Storage Component (see Fig. 1).

The remainder of this report is organized as follows: Section 2 summarizes the building and grid aggregator (GA) subsystems, discusses the new EV charging controller, and introduces the forecasting and storage components. The simulation environment, data correlation, and simulation use case used to generate results are then discussed in Section 3. The tracking performance of FAPC is analyzed in Section 4, followed by the robustness analysis and forecast importance in Section 5. Finally, the paper is summarized in Section 6.

## 2. Forecast-aided predictive control

As mentioned in Section 1.4, FAPC is an extension of the NALD algorithm [42,43]. Because the grid aggregator and building subsystems remain unchanged from [42] and [43], these subsystems are first briefly introduced. Then, the new EV charging controller is described in detail.
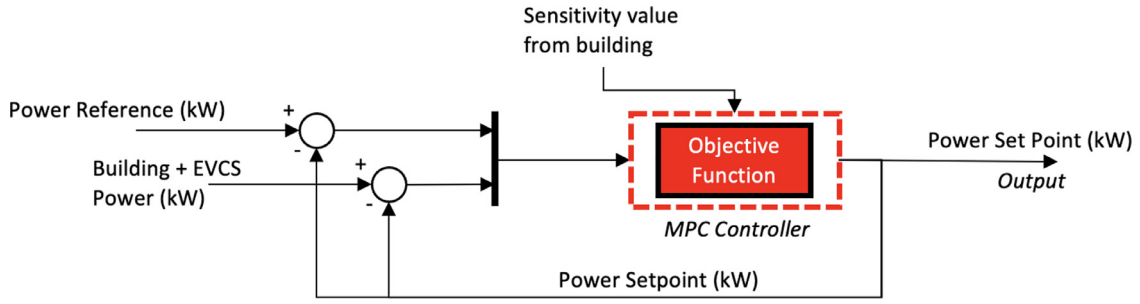
**Fig. 2.** Block diagram of the GA subsystem. The thick black line represents a mux operation where multiple vector signals are combined into a larger vector.

## 2.1. Building and grid aggregator subsystems

In limited communication-DMPC (LC-DMPC), an upstream subsystem's disturbance $Z$ is sent to a downstream subsystem. That downstream subsystem then returns a value indicating the effect of the upstream subsystem's disturbance on its local objective, the sensitivity $\gamma$. Received values $Z$ and $\gamma$ are injected into each subsystem's local objective function as the vectors $V$ and $\Psi$, respectively. Then, each subsystem $m$ solves its own local optimization problem, which can be stated generally as

$$
\begin{aligned}
min_{U_m} J_m = &\ e_m^T Q e_m + U_m^T S U_m + \Psi_m^T Z_m \\
\text{s.t.}\quad Y_m = &\ F_{y,m} x_{0,m} + M_{y,m} U_m + N_{y,m} V_m + P_{y,m} D_m \\
Z_m = &\ F_{z,m} x_{0,m} + M_{z,m} U_m + N_{z,m} V_m + P_{z,m} D_m \\
&\ \underline{U}_m \leq U_m \leq \bar{U}_m
\end{aligned}
\tag{1}
$$

where $e = r - y$ is the error vector, $r$ is the reference signal vector (typically a function of the incoming disturbance $V$) and $y$ is the subsystem's output vector. Here, $J$ is the local objective function where $U$ is the controllable input vector, $Q$ and $S$ are diagonal weight matrices corresponding to each penalty term in (1) (actual values shown in Table 4 in the Appendix), and $D$ is the external disturbance matrix. Note that in this work, $S$ is a matrix of zeros, and thus the second term is eliminated from (1). $F$, $M$, $N$, and $P$ are local model prediction matrices, and subscripts $(\cdot)_u$, $(\cdot)_v$, and $(\cdot)_d$ denote matrices corresponding to control inputs, upstream disturbances, and external disturbances, respectively. Most notable from (1) is the penalty term $\Psi_m^T Z_m$. This penalty term helps determine the leeway in the squared error term $e_m^T Q e_m$, eventually promoting convergence of the LC-DMPC algorithm to the centralized solution. To promote this convergence, subsystems communicate for multiple communication iterations between time steps. Note that time step and communication iteration superscripts are omitted in (1) for simplicity. Since this is an MPC-based algorithm, each variable represents that signal stacked across a vector with a length corresponding to the MPC horizon.

The next two subsections briefly describe the GA and building subsystems and how their individual physics-oriented models, control-based models, and objectives fit into the general LC-DMPC structure in (1). The authors refer the reader to reference [44] for details regarding LC-DMPC theory and stability analysis and to reference [45] for an application of LC-DMPC to distributed building control.

### 2.1.1. Grid aggregator

Fig. 2 shows a block diagram of the GA subsystem. This subsystem is a static system and thus assumes instantaneous dynamics with no physical model [45]. For the GA subsystem, (1) is implemented in the objective function block in Fig. 2. In general, the error vector $e$ for the GA subsystem contains $N + 1$ components

$$
e = \begin{bmatrix} P_{ref} - \sum_{m=1}^{N} P_{set,m} \\ P_{set,m} - P_m \\ \vdots \\ P_{set,N} - P_N \end{bmatrix}
\tag{2}
$$

where $P_{set,m}$ is the power set point sent to a downstream subsystem $m$, $P_m$ is the power output of subsystem $m$, and $N$ is the total number of subsystems directly connected to the GA. Conceptually, the GA subsystem works to distribute the bulk reference signal $P_{ref}$ to each of its neighbors while considering their individual needs. For results in this work, the building is the only downstream subsystem, and thus $N = 1$, $\sum P_{set,m} = P_{set,b}$, and $P_m = P_b$ where $P_b$ is the power consumption of the building.

### 2.1.2. Building

The building subsystem can be represented by the block diagram in Fig. 3. Like the GA subsystem, its local controller (i.e., MPC controller section in Fig. 3) also contains a two-component error vector $e$ as depicted by the mux component in Fig. 3:

$$
e = \begin{bmatrix} P_{set,b} - P_b \\ T_{ref} - T_b \end{bmatrix}
\tag{3}
$$

where $P_{set,b}$ is the power set point received from the GA subsystem, $P_b$ is the power consumption of the building, $T_{ref}$ is the desired internal building temperature (see Table 4 in the Appendix), and $T_b$ is the actual internal building temperature. Note that in addition to tracking $T_{ref}$, there are hard constraints on $T_b$ ($\underline{T}_b$ and $\bar{T}_b$), referred to as the comfort bounds.

To model the bulk building dynamics, a one-zone, 3-resistor 2-capacitor (3R2C) equivalent circuit model as shown in the plant section of Fig. 3 is used. This is a linear discrete-time dynamical model where the *states* are the internal and wall temperatures of the building, $T_b$ and $T_e$, the *outputs* are $T_b$ and $P_b$, and the *input* is the cooling load from the HVAC system in the building $Q_{HVAC}$.

$Q_{HVAC}$ is a function of the mass flow rate $\dot{m}$ and the supply air temperature $T_{sa}$ (i.e., $Q_{HVAC} = \dot{m}(T_b - T_{sa})$). $\dot{m}$ and $T_{sa}$ serve as inputs to the building's air handling unit (AHU). These inputs are additionally used in the AHU Model block in the plant section of Fig. 3 to estimate the power consumption of the building. Using equations and parameters derived in [45] along with the 3R2C model, the three inputs $Q_{HVAC}$, $\dot{m}$, and $T_{sa}$ are used to determine the building subsystem outputs $T_b$ and $P_b$.

To make predictions across the MPC horizon, a more simple linear parametric model is identified from the 3R2C model. This is referred to as the control model and is located directly below the Objective Function block in the MPC controller section of Fig. 3. Here, the only state is the internal temperature. The power dynamics are not considered. Because the computation for $Q_{HVAC}$ is bilinear, the control model is linearized about the current building temperature $T_b$ at each discrete time step. For more details on the 3R2C model and linear parametric model, the reader is referred to [45].

## 2.2. Electric vehicle charging station subsystem

In this section, the new EV charging control algorithm is introduced. The novelty of this algorithm is in its objective function, where an EV day-ahead plan (EVDAP) is tracked in real time. The computation of this plan is discussed in more detail in Section 2.3.
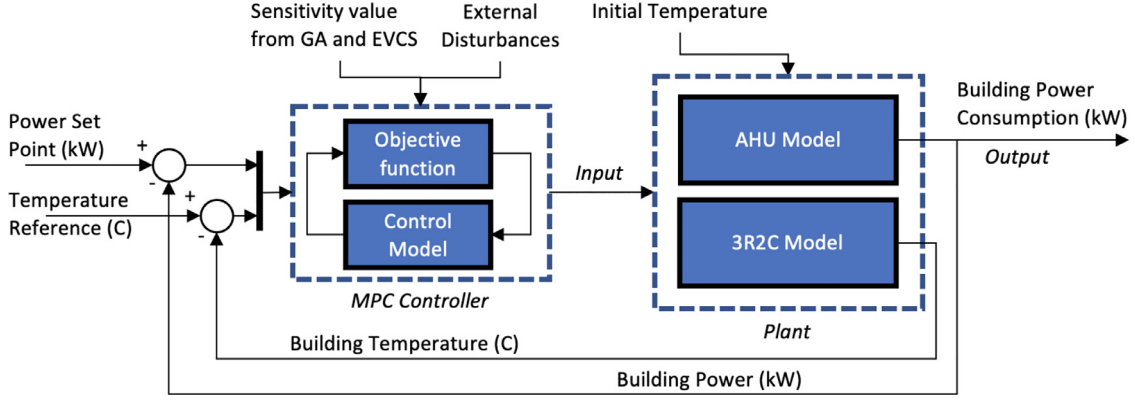
**Fig. 3.** Control system block diagram of the building subsystem.
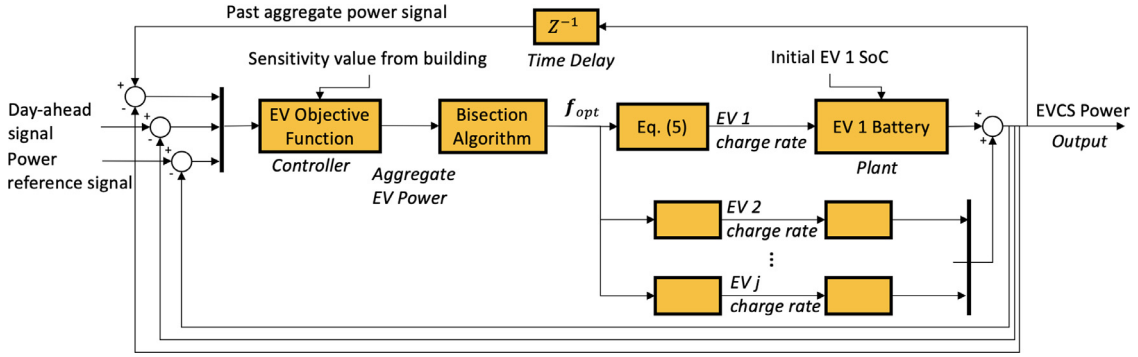


**Fig. 4.** Block diagram of the updated EVCS controller.

Fig. 4 shows the block diagram for the EVCS subsystem. First, three signals (past aggregate EV load, forecasted aggregate EV load, and power reference signal) are passed to the EV Objective Function block. The EV Objective Function block serves as the controller for the EVCS subsystem and computes the optimal aggregate EV load at time $t$ and communication iteration $k$, $P^{t,k}$, by solving the optimization problem

$$\min_{P^{t,k}} f\left(P^{t,k}\right) = \underbrace{\omega_1\left(P^{t,k}_{rt-track} - P^{t,k}\right)^2}_{\text{Component 1}} + \underbrace{\omega_2\left(P^{t-1} - P^{t,k}\right)^2}_{\text{Component 2}}$$

$$+ \underbrace{\omega_3\left(P^{t+1}_{EV,DA} - P^{t,k}\right)^2}_{\text{Component 3}}$$

$$+ \underbrace{\omega_4 \max\left\{P^{1:t}_{EV}, P^{t,k}, P^{t+1:T}_{EV,DA}\right\}}_{\text{Component 4}} + \underbrace{\omega_5 \Psi^{t,k} P^{t,k}}_{\text{Component 5}}$$

$$\text{s. t. } P^{t,k}_{lb} \leq P^{t,k} \leq P^{t,k}_{ub} \tag{4}$$

Note that, unlike in (1), the time step and communication iteration superscripts are included in (4) for ease of understanding the different signals.

The objective function in (4) has five different components: 1) the power reference tracking component, 2) the previous time step's aggregate power tracking component, 3) the EVDAP tracking component, 4) the peak load minimization component, and 5) the sensitivity component. Component 1 tracks an augmented reference signal $P_{rt-track} = P_{set,b} - Z_b$. Component 2 serves as a smoothing parameter, limiting the change in charging rate from one time step to the next. The power signal delayed by one time step is fed back to the controller through the time delay block in Fig. 4. Component 3 tracks the next time step value in the EVDAP $P_{EV,DA}$. Loosely inspired by work in [46], the *previous* $(t-1)$ and *next* $(t+1)$ time step tracking in Components 2 and 3, in a sense,

pull and guide the trajectory of (4) through time. Component 4 imposes a penalty on the peak load of the aggregate EV charge load. This maximum peak load includes either a past observed peak, $P^{1:t}$, the current consumption, or a future forecasted peak, $P^{t+1:T}_{EV,DA}$. Last, Component 5 is the sensitivity penalty. Components 1–5 each have their own associated weight $\omega$, which can be arbitrarily selected based on user preferences. We note that different choices of $\omega$ will result in different outcomes of (4) due to the conflicting nature of each component. Therefore, careful choices of $\omega$ will dictate the user's desired balance between components. The weight values used in this work are shown in Table 4 in the Appendix.

While (4) acts as the controller in Fig. 4 for the EVCS subsystem, it only computes the optimal *aggregate* charging load for the EVCS at time $t$ (and communication iteration $k$). To compute the optimal *individual* charging rates of each EV $p^t_j$, the relation in (5) is applied to each EV $j$ in the set of EVs currently plugged in $\mathcal{J}$. Here, superscripts $(\cdot)^a$ and $(\cdot)^d$ represent arrival and departure indices, respectively. $T$ represents a fixed time ($T$ is the simulation length, $T^a$ is the arrival time, and $T^d$ is the departure time), $SoC$ is the state of charge, $\Delta_T$ is the discrete time step, and $\bar{p}$ is the maximum charge rate.

$$p^t_j(f) = \left[\frac{1}{\Delta_T}(SoC^d_j - SoC^a_j) - (T^d_j - t)(\bar{p}_j - f)\right]^{\bar{p}_j}_0 \forall j \in \mathcal{J} \tag{5}$$

Equation (5) ensures that each EV is fully charged upon its departure time while maintaining flexibility for each EV in the future by use of a flex parameter, $f$. In (5), the individual charging rates are a function of the flex parameter where a large $f$ represents more flexibility and vice versa. The first term in (5) is the total power each EV must consume by its departure time. The second term represents the deviation from this total power as a function of the flex parameter (i.e., the optimal charging rate between 0 and $\bar{p}_j$). Since $f$ is the only parameter in (5) not fixed at time $t$, as $f$ increases, the second term decreases. If the second term is smaller, then the charging rate to apply, $p^t_j(f)$, is larger and vice versa.

Therefore, $p_j^t(f)$ monotonically increases as a function of $f$, and thus simple bisection is used to determine the optimal flex parameter $f_{opt}$ as shown in Algorithm 1 in the Appendix. Note that $f_{opt}$ is the same across all EVs and thus equalizes the amount of flexibility among all EVs. After the individual charging rates are determined ("Eq. (5)" in Fig. 4), the $SoC$ of each EV battery is updated in the Plant block. Note that the sum of each charging rate $p_j$ must equal the "aggregate EV power" signal shown in Fig. 4) determined by (4), as this serves as the "EVCS power" output of the EVCS subsystem.

In order to coordinate with the building and GA subsystems, we incorporate the EVCS subsystem into the LC-DMPC framework. Instead of having the form of (1), the combination of (4) and (5) is used as the local objective. However, the same information is communicated between the EVCS subsystem and building subsystem. Specifically, $P_{rt-track}^{t,k} \equiv V$, $\Psi^{t,k} \equiv \Psi$, $P^{t,k} \equiv Z$, and the sensitivity sent to the building subsystem is computed using

$$\gamma = \frac{(f(P^{t-1,k}) - f(P^{t,k}))}{(P_{rt-track}^{t-1,k} - P_{rt-track}^{t,k})} = \frac{\Delta f}{\Delta P_{rt-track}} \equiv \frac{\partial J}{\partial V} \tag{6}$$

### 2.3. Forecast component

An important contribution of this work is the Forecast Component. While the building and GA subsystem control actions are determined through receding horizon control (i.e. MPC) with respect to *forecasted disturbances*, EV charging controllers in [42] and [43] solve for a real-time control action with respect to *current disturbances* only. However, this new EV charging control algorithm uses an offline-computed EVDAP as a guide. This enables the real-time control policy to be informed of future disturbances. A similar strategy for EV charging control of an entire province was shown in [47] and is an inspiration for this EVDAP.

This EVDAP $P_{EV,DA}$ is the "optimal" charging plan for a given day computed offline before the real-time simulation and is represented by the Forecast Component on the bottom left of Fig. 1. It should be noted that perfect knowledge of the charging events for a succeeding day is assumed, providing an upper bound to the optimality of the EVDAP. This provides a metric to compare the stochastic and uncertain nature of EV charging event forecasting, which will be investigated in future work. However, the impact of imperfect forecasts is investigated in Section 5.2. A note on terminology: we refer to the EVDAP as a *plan* and not a *forecast* because the EVDAP is not a forecast itself. However, the specific charging events, neighboring building load, and RE generation are indeed *forecasts* and are used to shape the EVDAP.

There is a two-step process to compute the EVDAP profile $P_{EV,DA}$. In the first step, an initial EVDAP is computed using a building load forecast $P_{B,DA}$, a RE generation forecast $P_{RE,DA}$, and a forecasted list of charging events. These perfectly known charging events include arrival $SoC$ and time ($SoC^a$ and $T^a$) as well as departure $SoC$ and time ($SoC^d$ and $T^d$) for all EVs $j \in \mathcal{J}$. This initial EVDAP is computed by solving

$$\min_{P_{EV,DA}, L} \max_{t\in\mathcal{T}}\{L^t\} + \frac{1}{T}\sum_{t=1}^{T}\left(L^t - L^{t-1}\right)^2 \tag{7a}$$

$s.t$

$$L^t = P_{EV,DA}^t + P_{B,DA}^t - P_{RE,DA}^t, \forall t \in \mathcal{T} \tag{7b}$$

$$P_{EV,DA}^t = (1/\Delta_T)(E_{EV,U}^t - E_{EV,U}^{t-1}), \forall t \in \mathcal{T} \tag{7c}$$

$$E_{EV,U}^t = \sum_{j=1}^{t}\sum_{i=1}^{\mathcal{J}^t}\Delta_T p_i^j, \forall t \in \mathcal{T} \tag{7d}$$

$$\sum_{i=1}^{\mathcal{J}_i^{t,d}}(SoC_i^d - SoC_i^a) \le E_{EV,U}^t \le \sum_{i=1}^{\mathcal{J}_i^{t,a}}(SoC_i^d - SoC_i^a), \forall t \in \mathcal{T} \tag{7e}$$

$$0.0 \le P_{EV,DA}^t \le \sum_{i=1}^{\mathcal{J}^t} \le \bar{p}_i, \forall t \in \mathcal{T} \tag{7f}$$

where $L^t$ is the net load at time $t$, $P_{EV,DA}^t$ is the aggregate EV load at time $t$, $E_{EV,U}^t$ is the total energy consumed by the EVCS by time $t$, $\mathcal{J}^{t,a}$ is the set of EVs that arrived at or before time $t$, $\mathcal{J}^{t,d}$ is the set of all EVs that have arrived and then departed by time $t$, and $\mathcal{J}^t$ is the set of all EVs that can be charged at time $t$. To clarify, constraint (7e) constrains the total energy consumed by the EV's currently plugged in from time 0 to $t$. The bounds of this constraint represent the energy usage by all EVs that have completed their charging cycle by time $t$ and the energy usage by all EVs that the EVCS has seen by time $t$. Last, $T$ is the total simulation length (1440 minutes), and $\mathcal{T} = \{1, 2, \dots, T\}$.

For the second step of the process, the reader is referred to Algorithm 2 in the Appendix, but a brief explanation is provided here. Using the same forecasted charging events as in the first step, another plan $P_{rt}$ is computed using (4) and (5) where $\omega_1 = \omega_5 = 0$ and $P_{EV,DA}$ computed in (7) is used in Component 3 of (4). This step ensures individual charging event constraints are satisfied, resulting in a feasible EVDAP. $P_{rt}$ and $P_{EV,DA}$ are then compared where any mismatch between them at a time $t$ is reflected in the variable $P_{diff}^t$. A series of iterative steps are then taken to find the vector $\delta$ that most effectively shifts the load forward in time until the EVDAP is both feasible and adequately smooth. This vector $\delta$ is then added to the initial EVDAP, or $P_{EV,DA} = P_{EV,DA} + \delta$, to obtain an optimal and feasible EVDAP.

From constraint (7b), it can be seen that the net load $L$ is composed of a neighboring building load forecast $P_{B,DA}$ as well as a RE generation signal forecast $P_{RE,DA}$. To compute an accurate EVDAP, these profiles must be estimated. The following sections highlight the strategies used to do so.

### 2.3.1. Building load forecast

It is possible to obtain a building load forecast using a greedy building controller subject to forecasted disturbances. These forecasted disturbances (outdoor air temperature, solar irradiation, and building occupancy) are assumed to be perfectly known in the generation of this forecast and, like the EVDAP, provide an upper bound on the building forecast confidence. Investigating the stochastic nature of these disturbances is a topic of future work. This greedy controller tracks only the reference temperature (i.e., the error vector is $e = [T_{ref} - T_b]$). As compared to (1), the sensitivity component and horizon length are removed from the problem. A resulting simple, real-time optimization problem subject to the building dynamics $f_b(\cdot)$ and control input constraints remains. This problem is equivalent to removing the control model, the AUH model, the MPC controller section, and the building power feedback loop in Fig. 3. Running this simplified optimization problem across an entire day using forecasted external disturbances (weather data), a forecasted building load can be obtained. This greedy controller is shown in (8):

$$\min_{u_1^t, u_2^t} \{(T_{ref} - T_b^t)^2 + (U^t - U^{t-1})^T\Lambda(U^t - U^{t-1})\}$$
$$s.t. \quad T_b^t = f_b(u_1^t, u_2^t, d^t, T_b^{t-1})$$
$$\underline{u}_1 \le u_1^t \le \bar{u}_1$$
$$\underline{u}_2 \le u_2^t \le \bar{u}_2$$
$$\underline{Q}_{HVAC} \le u_1^t(u_2^t - T_b^{t-1}) \le \bar{Q}_{HVAC} \tag{8}$$

where $U = [u_1\ u_2]^T$ is the control input vector, $\Lambda = diag(\lambda)$ holds the penalties on changing control actions, and $d$ is the disturbance vector. $u_1$ and $u_2$ are the inputs to the model and correspond to the mass flow rate $\dot{m}_s$ and supply air temperature $T_{sa}$, respectively. A $(\bar{\cdot})$ or $(\underline{\cdot})$ represents an upper or lower bound on a variable, respectively. The values used for the constraint parameters and weights are shown in Table 4 in the Appendix. An example of a building load forecast as a result of running (8) for a day is displayed in Fig. 5.

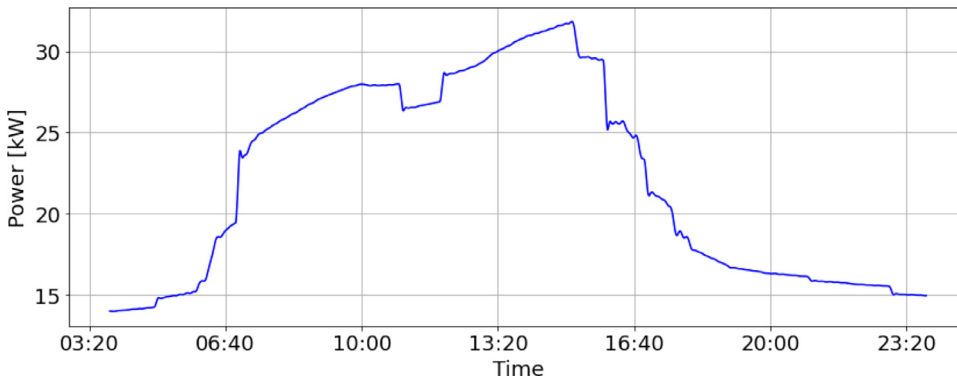**Fig. 5.** Building load forecast output from (8) based on forecasted building occupancy profile and forecasted disturbances.
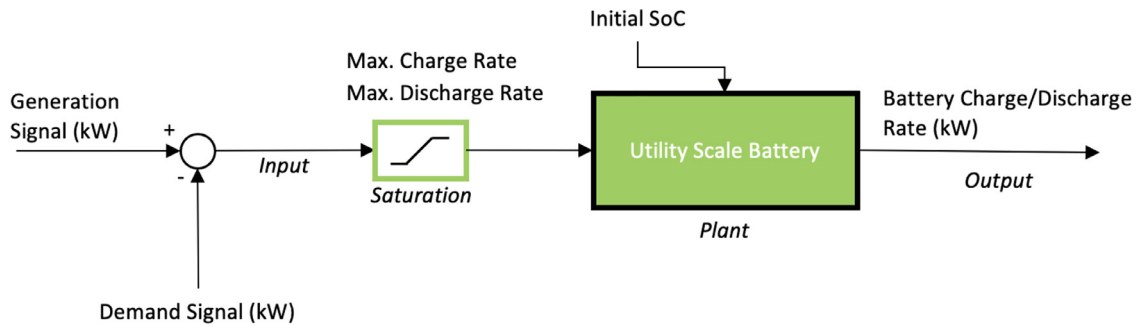


**Fig. 6.** Block diagram of the simple storage controller used to compute the amount of storage power dispatched to the system at each time step.

### 2.3.2. RE generation forecast

Assuming a weather forecast is available, the solar and wind generation profiles for the succeeding day can be estimated. Like in the building forecast, the weather data to generate the RE generation forecast is assumed perfectly known to provide an upper bound on the forecast confidence. Including uncertainties associated with weather forecasts will be less confident, can be compared to the perfect forecast, and are a topic of future work. With a forecast of the global horizontal irradiance (GHI) profile $\dot{Q}_{GHI}$ at a certain location and date, a solar power generation profile can be estimated using the simple equation

$$P_{solar} = \dot{Q}_{GHI} * A * \eta \tag{9}$$

where $A$ is the area that the solar panels occupy and $\eta$ is the efficiency of the solar panels (see Table 4 in the Appendix). Note that it is assumed that the solar panels are pointed directly into the sun throughout the day.

Additionally, with a forecast of the wind speed profile at the same location and date, the NREL wind farm simulation tool FLOw Redirection and Induction in Steady state (FLORIS) [50] can be used to estimate the wind power generation. Note that FLORIS can simulate a single turbine or an entire wind farm and also easily models the turbine's cut-in wind speed, rated wind speed, and cut-out wind speed. Because the system in this work is small, only one turbine is considered. Because of this, the use of an entire wind farm analysis tool may be more than what is needed, but future work for larger systems will take advantage of FLORIS' multiturbine simulation capabilities. Like the solar generation, we assume the turbine is pointed directly into the wind for all time.

### 2.4. Storage component

Figure 6 shows the simple storage component, seen as the green block in Fig. 1. The storage component is not integrated into the FAPC algorithm (i.e., it is not a subsystem in the FAPC algorithm). The purpose of the storage component is to estimate the size of the BESS needed to deploy in order to perfectly track the RE generation signal.

Figure 6 shows the simulation model of the BESS used to calculate the battery charge and discharge rates at each time $t$. First, the difference between the total demand and RE generation is computed and used as the input to the battery plant. This value represents the amount of charging or discharging requested from the BESS at time $t$. This charge or discharge rate is then saturated depending on the physical limits of the BESS (i.e., the maximum charge or discharge rate and current $SoC$). Depending on the initial battery $SoC$ as well as the amount of charging or discharging applied at time $t$, the $SoC$ of the battery is then updated at each time step in the "Utility Scale Battery" plant box. The output of the battery system is the charge or discharge rate and represents the amount of power dispatched by the battery to the system at time $t$.

### 3. Simulation environment

Because each subsystem in FAPC is affected by external disturbance data and causal events, it is important to ensure all factors are correlated to draw legitimate conclusions from results. In this simulation, there are two major sources of raw data: 1) weather data (wind speed, solar irradiation, and outdoor air temperature), and 2) building occupancy data (see the blue blocks in Fig. 7). These data are either used directly in different models or used to generate other data that are ultimately used for different parts of FAPC. Fig. 7 displays how the raw data are utilized in different components of FAPC. In the next sections, different aspects of the correlated simulation environment are described.

### 3.1. Building occupancy and charging events

In this work, it is assumed that the EVCS is connected to a commercial building where the EV owners are the occupants in the building. As mentioned in Section 3, raw data consist of building occupancy profiles for a given day. Fig. 8 shows the building occupancy count at each hour as the black line in the top subplot. While the specific arrival and departure of each occupant is unknown, these data provide a rough estimate of the EV charging events.
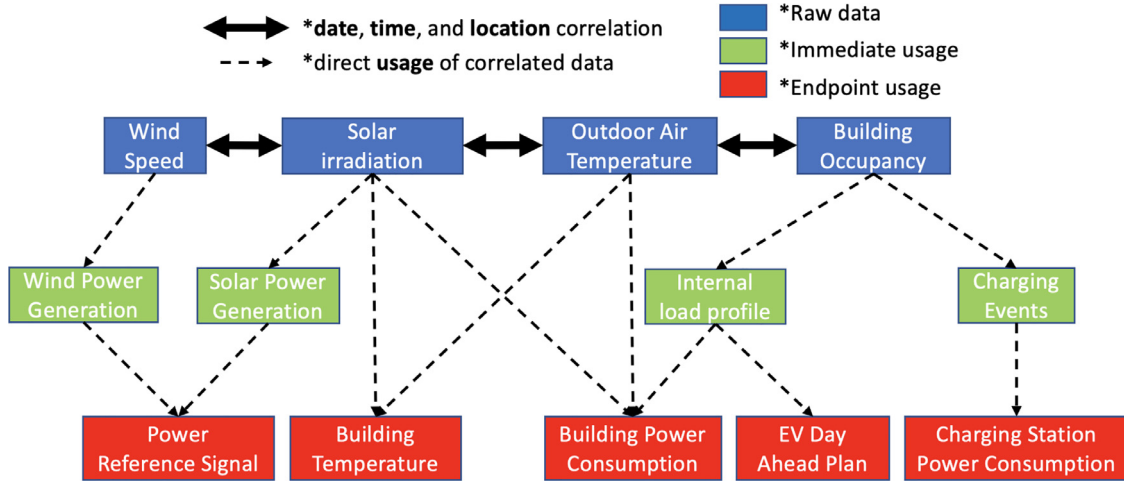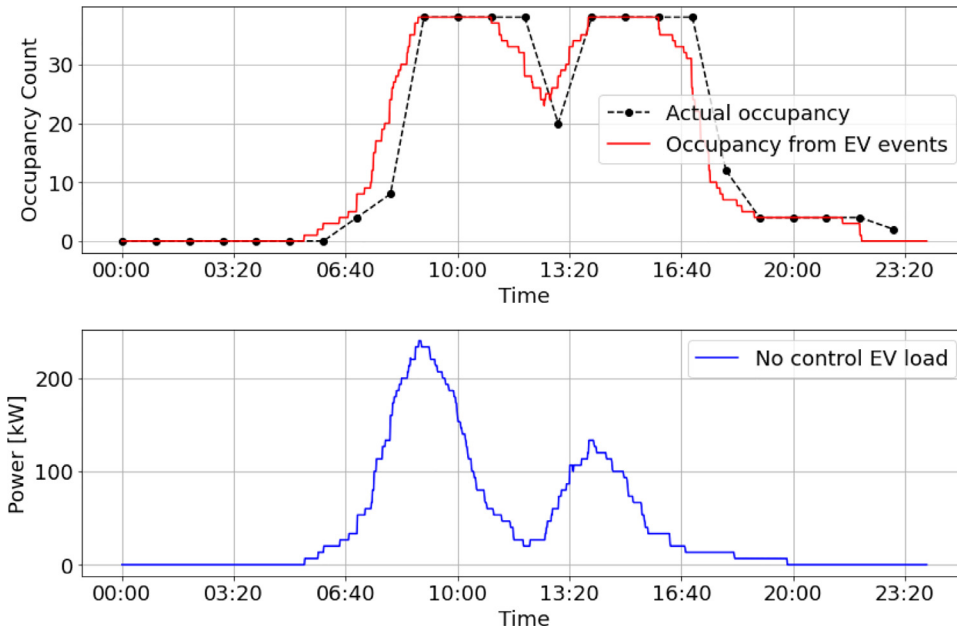
**Fig. 7.** Data correlation schematic.



**Fig. 8. Top**: Building occupancy profile from building occupancy data (black) and building occupancy from selected EV charging (red). **Bottom**: Baseline control EV load profile based on selected EV charging event data. (For interpretation of the references to colour in this figure legend, the reader is referred to the web version of this article.)

Assuming each occupant is driving an EV to work, EV events are randomly chosen (from a large pool of precomputed charging events) such that they align with the building occupancy schedule. This large pool of precomputed events are generated by the EVIpro simulation platform [48]. Fig. 8 shows the occupancy profile as defined by the charging events by assuming the building occupancy increases by 1 unit at an arrival time and decreases by 1 unit at a departure time.

Last, the chosen set of charging events is used to obtain a baseline control load profile. This represents the aggregate EV charging load profile when each EV applies its maximum charging rate $\bar{p}$ upon arriving at the EVCS. This profile is shown in the bottom of Fig. 8.

### 3.2. Disturbances and generation

As discussed in Section 2.3, RE generation signal is made up of both solar and wind generation. Using the National Solar Radiation Database (NSRDB) [49], solar irradiation and wind data is extracted near where the building is located (near Denver, Colorado). Solar and wind generation profiles are then computed using (9) and the FLORIS tool [50], respectively. Note that the aggregate RE generation profile is scaled to match the size of the system.

Fig. 9 shows the solar irradiance, solar generation, wind speed, and wind generation profiles for the same date and time. Note that $\dot{Q}_{GHI}$ is also used as a disturbance in the building simulation and control models.

### 3.3. Simulation setup

Before running different cases and analyzing results, the specific scenario considered for the results is introduced. Using the dates of July 8, 11, and 28, 2019, from 3:50 to 23:50, the simulation environment described in Sections 3.1 and 3.2 is set up. By using this time frame, we include all charging events and times when occupants are in the building. With the specified date and time determined, load forecasts $P_{B,DA}$ and $P_{EV,DA}$ are computed, and the RE generation signal $P_{RE,DA}$ is scaled to an appropriate size for the specific scenario. To do so, the total forecasted energy demanded from the building ($E_{B,DA}$) and EVCS ($E_{EV,DA}$) as well as the total forecasted energy generated from the solar and wind ($E_{RE,DA}$) are computed by taking the integral of their corresponding load forecasts $P_{B,DA}$, $P_{EV,DA}$, and $P_{RE,DA}$. A scaling factor $\alpha$ to appropriately size $P_{RE,DA}$, or $P_{RE,DA} \leftarrow \alpha * P_{RE,DA}$, is then computed using
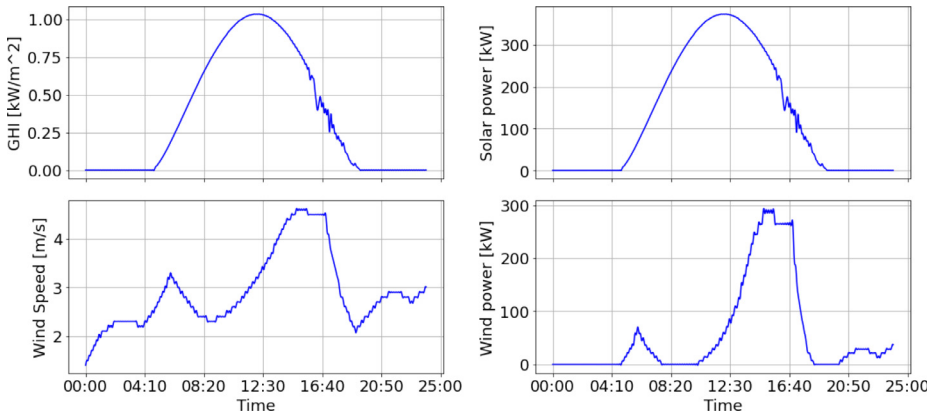
$$\alpha = (E_{B,DA} + E_{EV,DA})/E_{RE,DA} \tag{10}$$

**Fig. 9. Top Left**: Solar irradiance profile on July 11, 2019, from the NSRDB [49]. **Top Right**: Solar power generation profile corresponding to the irradiance profile and Eq. (9). **Bottom Left**: Wind speed data on July 11, 2019, from the NSRDB [49]. **Bottom Right**: Wind power data corresponding to the wind speed data on the right. The profile is generated using FLORIS.

**Table 1**

Summary of the five different control scenarios analyzed in the control scenario comparison.

| Control Scenario | Baseline Building Control | Baseline EVCS Control | Optimal Building Control | Optimal EVCS Control | Coordination |
|---|---|---|---|---|---|
| 1 | X | X | - | - | - |
| 2 | X | - | - | X | - |
| 3 | - | X | X | - | - |
| 4 | - | - | X | X | - |
| 5 | - | - | X | X | X |

## 4. Control scenario comparison

In this section, the tracking performance of the FAPC algorithm is analyzed. To do so, we apply FAPC to the simulation environment described in Section 3 for July 11, 2019. Then, five separate control scenarios, organized in Table 1, are analyzed: 1) baseline control, 2) optimal EV charging control only, 3) optimal building control only, 4) optimal EV charging control and building control with no coordination, and 5) fully coordinated and optimal EV charging and building control (FAPC). Note that in the four uncoordinated scenarios, the sensitivity value is not passed between subsystems. The performance of the FAPC algorithm is then quantified by analyzing the size of the utility-scale BESS necessary for perfect tracking.

In Scenario 1, both the building and the EVCS are using their corresponding baseline controller. For the building subsystem, the baseline controller is described in Section 2.3.1, resulting in a profile similar to what is shown in Fig. 5. For the EVCS subsystem, the baseline controller charges each EV at its maximum charging rate as soon as they arrive at the EVCS, similar to the profile shown in the bottom plot in Fig. 8.

The top plot in Fig. 10 shows results from Scenario 1. As expected, since there is no optimal control in place for either subsystem, the total demand does not track the RE generation signal. Largely influenced by the EV charging load, there are large errors in the tracking near 9:00, 12:00, and 16:00. Because of this, a BESS with a large power and energy capacity is needed to perfectly track the RE generation signal. The instantaneous BESS power at each time step is depicted by the green line in the top plot of Fig. 10.

In both Scenarios 2 and 3, the tracking is indeed improved over Scenario 1. However, the improvement is much more obvious in Scenario 2. This is expected since the EVs occupy a larger percentage of the total demand and the EVs have much more flexibility than the buildings (i.e., the building must satisfy strict physical constraints such as temperature comfort bounds). Additionally, because we consider a commercial building, we assume that the EVs are plugged in all day, further increasing their flexibility.

In Scenario 4, both building and EVCS subsystems are controlled using FAPC with no coordination, i.e., the sensitivity component is not included in either of the subsystems' local objective functions. Visually, in Figs. 2–4, the sensitivity value from a neighboring subsystem is not entering the controller block. The second to bottom plot in Fig. 10 shows that the tracking performance is much improved over Scenarios 1 and 3. However, it is comparable to Scenario 2 (optimal EV charging control only). This improvement in performance is expected as both subsystems are optimally controlling their demand based on the available generation. However, each subsystem is only optimizing locally, and does not take into account the preference or need of the other subsystem (coordination). While this lack of coordination may not appear to be a large issue in this specific scenario, it may have more of an impact when the number of subsystems increase.

Last, in Scenario 5, both the building and EVCS subsystems are controlled through FAPC with full coordination (sensitivity signals are present in each of Figs. 2–4). Albeit somewhat noisy, Scenario 5 clearly outperforms Scenarios 1 - 4 (in terms of tracking). This results in a much smaller required BESS power and energy capacity in the system, considerably reducing the amount of charging and discharging as depicted by the green line.

Next, we show the improvement in performance from Scenario 1 - 4 by estimating the required amount of BESS to allow perfect tracking. Here, it is assumed that the maximum charge or discharge rate is equal to the power capacity, and thus, charge or discharge saturation. The power capacity is simply the largest tracking error between the demand and generation in each scenario shown in Fig. 10. The top plot in Fig. 11 shows the power capacity for each scenario in Table 1. The bottom plot displays the total energy charged and discharged by the BESS during the simulation.

From the top plot in Fig. 11, it can be seen that, apart from Scenario 2, power capacity (kW) decreases from Scenario 1 to Scenario 5. Specifically, there is a reduction in BESS power capacity of 47.3% from Scenario 1 to 5. While Scenario 2 requires less power capacity than in Scenarios 3 and 4, the BESS power capacity is still reduced from Scenario 2 to 5. A similar result is shown in the reduction of charging and discharging occurring throughout the simulation, which is reduced by 71.0% and 82.7% from Scenario 1 to 5, respectively. This information plotted in the bottom plot of Fig. 11.

To further investigate the implications of this result, the required BESS size is estimated. Typically, a BESS is sized by both its power capacity (kW) and energy capacity (kWh). To size the utility-scale BESS in this work, we simply multiply the previously found power capacities by time, or the storage duration. To find the optimal storage duration, we incrementally scale the storage duration until perfect tracking is achieved. Note that a battery is a causal system and thus the initial $SoC$ will drastically change the required battery size. In this work we assume an initial $SoC$ of 0.5, resulting in a BESS size reduction of 79.9% from Scenario 1 to 5.
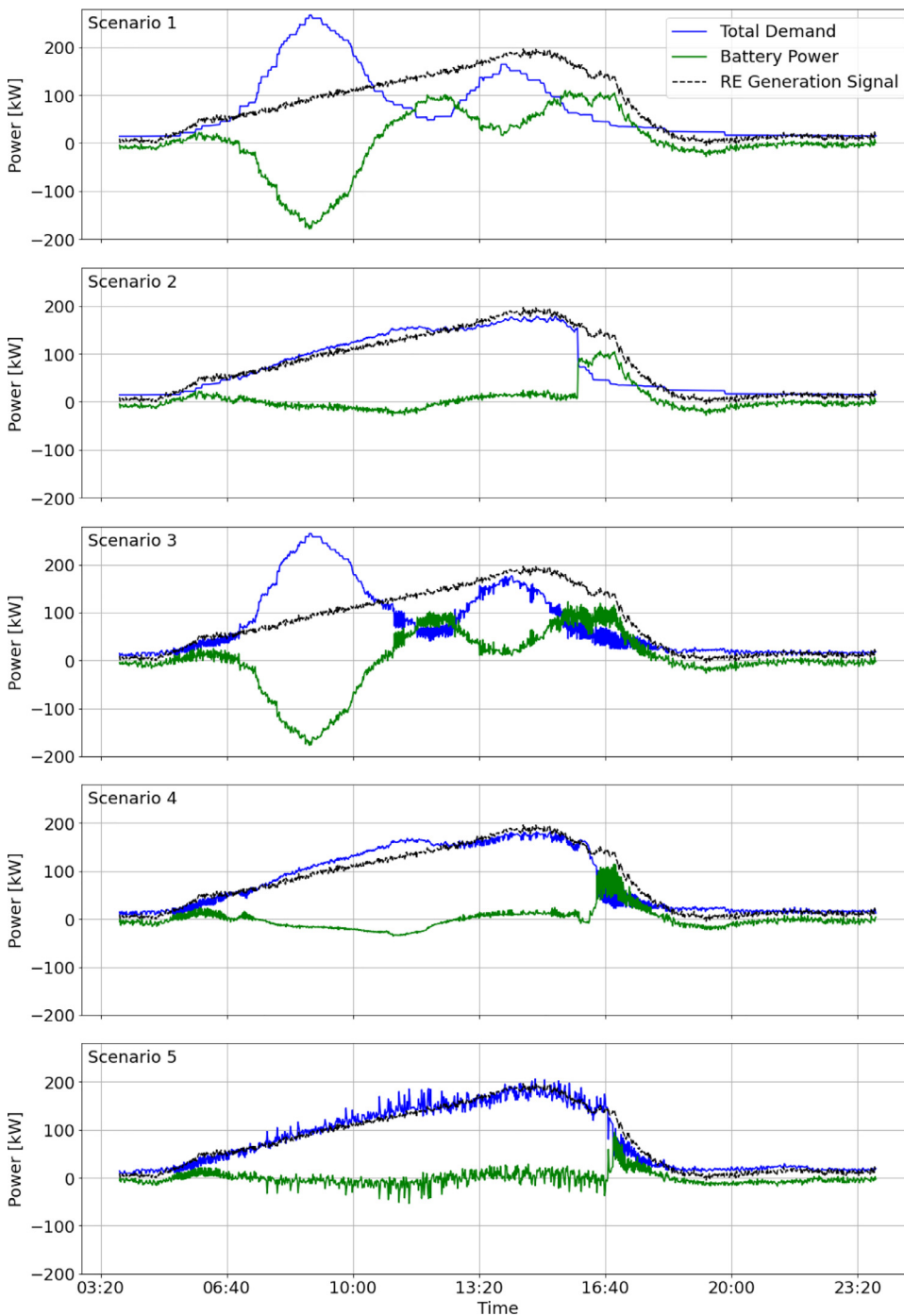
**Fig. 10.** The tracking performance of the FAPC algorithm discussed in this report in each scenario described in Table 1. For each scenario, the RE generation signal is the black dashed line, the total demand signal is the blue line, and the amount of battery power required to match the load and generation is the green line. (For interpretation of the references to colour in this figure legend, the reader is referred to the web version of this article.)

Last, the authors note that in Scenarios 2, 4, and 5 of Fig. 10, the BESS is predominantly sized by a spike near 16:40. Such a short duration spike could be mitigated using a potentially less expensive storage device such as a flywheel, even further reducing the required BESS size. The inclusion of other types of storage is a topic of future research.

## 5. Robustness analysis

The results in Section 4 show a substantial reduction in power capacity, charging and discharging energy, and BESS size required to enable perfect tracking of the RE generation. Note that this was done for a single day with a smooth, reliable solar generation signal. In this section, the robustness of the FAPC algorithm in different scenarios is examined. Three test days are considered, as outlined in Table 2.

**Table 2**
Three test days considered in the robustness analysis. Test Day 1 uses the same results from Scenarios 1 and 5 in Fig. 10.

| Day | Weekend/Weekday | Weather Type | Connection to Fig. 10 |
|-----|-----------------|--------------|------------------------|
| 1 | Weekday | Sunny | Control Scenario 1 and 5 |
| 2 | Weekday | Intermittent Clouds | None |
| 3 | Weekend | Sunny | None |

The tracking performance of the FAPC (Scenario 5) with respect to the baseline control scenario (Scenario 1) in each of the three test days is shown in Fig. 12. The top plot of Fig. 12 displays the tracking performance of the FAPC algorithm for a completely sunny weekday (Day
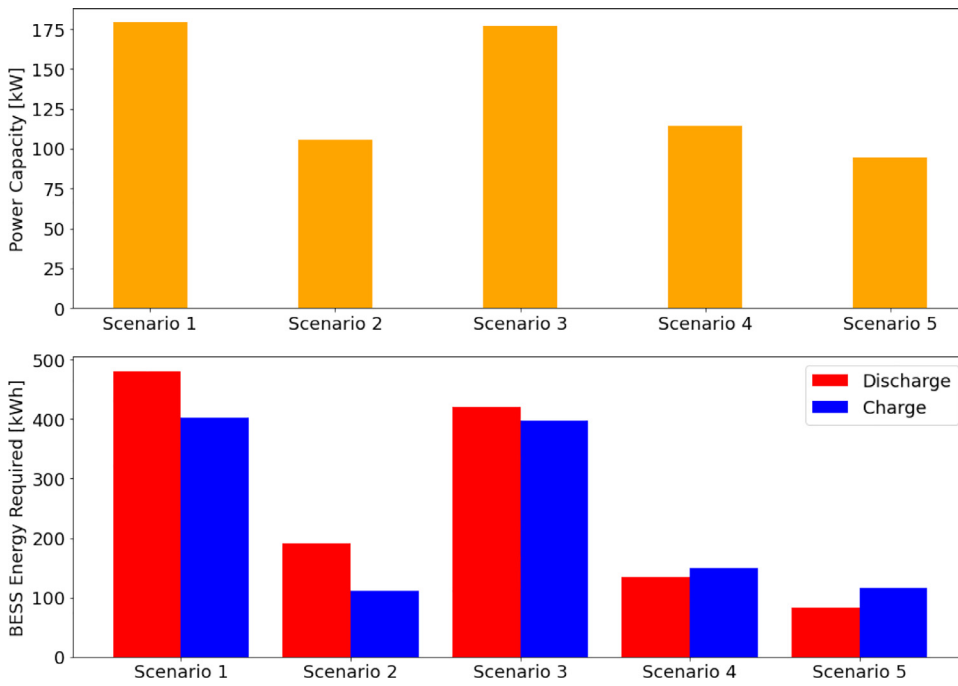
**Fig. 11.** Analysis of storage usage in each case. **Top**: Minimum BESS power capacity needed for perfect tracking in the system for each case. **Bottom**: Charging (blue) and discharging (red) energy throughout the simulation for each case. (For interpretation of the references to colour in this figure legend, the reader is referred to the web version of this article.)
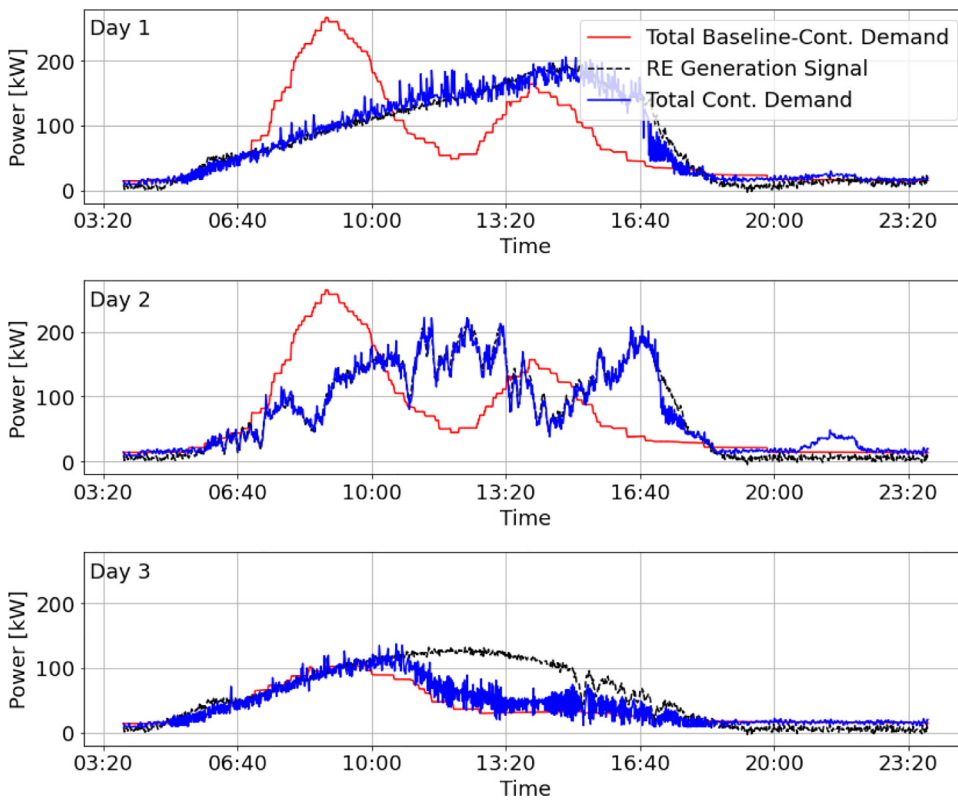


**Fig. 12.** FAPC controller performance comparing the total baseline controlled demand (red) and the total controlled demand (blue) to the RE generation signal (black dashed) for **Top:** a perfect solar day (Day 1), **Middle:** a bad solar day (Day 2), and **Bottom:** a weekend (Day 3). (For interpretation of the references to colour in this figure legend, the reader is referred to the web version of this article.)

1). The red line is the total baseline controlled demand while the blue line is the total demand that has been shifted by FAPC. Note that this is the same result shown in the top and bottom subplots of Fig. 10, with the red curve representing Scenario 1, the blue curve corresponding to Scenario 5, and the BESS power signal omitted.

The middle plot of Fig. 12 displays results for Day 2. Here, the solar generation is much more intermittent (i.e., there are clouds passing over during the day). This intermittency is reflected in the large fluctuations in the RE generation signal. While the RE generation signal fluctuates much more than in Day 1, the FAPC-controlled demand continues to track the RE generation signal very well in comparison to the baseline-controlled demand. The only demand/generation mismatch appears near time 16:40, where a large drop in the demand occurs. This mismatch is most likely due to either multiple EVs reaching their departure times or reaching their desired states of charge. Note that since the occupancy profiles are the same as in Day 1 (both weekdays), the building's internal load is identical. Any difference in total demand comes through the difference in outdoor disturbances.
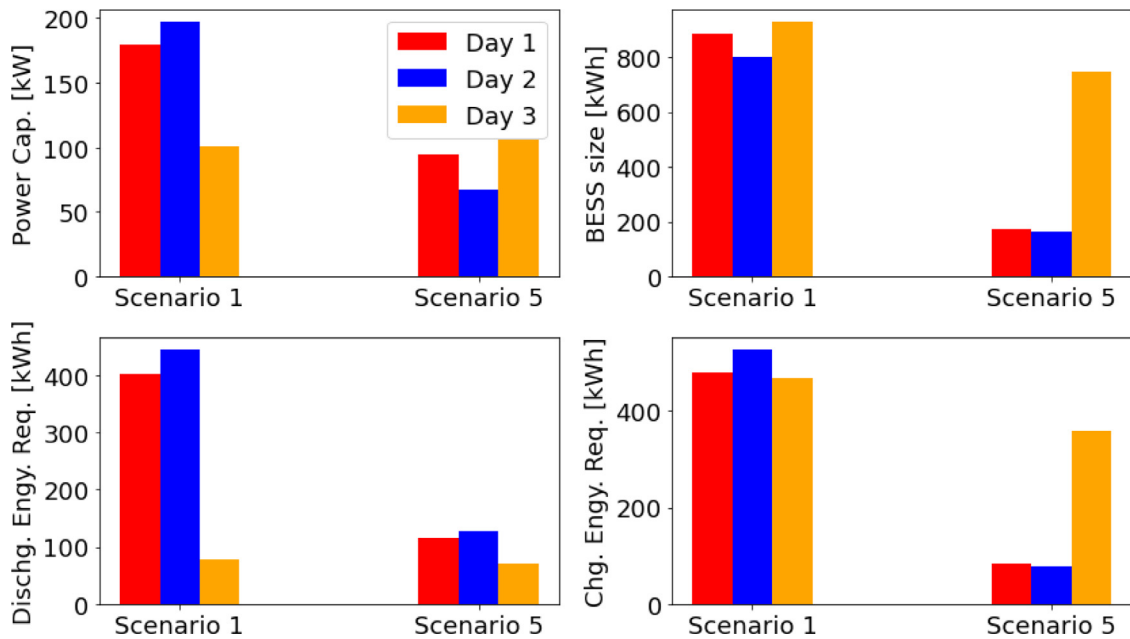
**Fig. 13. Top Left:** BESS power capacity (kW). **Top Right:** BESS size (kWh). **Bottom Left:** Discharging energy (kWh). **Bottom Right:** Charging energy (kWh) for the baseline-controlled and controlled cases in each of the three days.

The bottom plot of Fig. 12 displays Day 3, of which the RE generation signal is relatively smooth, but the simulation day is a weekend. Hence, the occupancy schedule for the building is different, resulting in a reduced demand by both the building and EVs. Although the FAPC algorithm does shift demand, the tracking is much worse than in other scenarios since there is not enough load to match the generation. Note that in the previous two cases, the EV demand occupies roughly 70% of the total demand, allowing the EV controller to shift demand more easily. However, because the EV demand is much lower on the weekend, its flexibility is decreased, and the total demand cannot be shifted as effectively compared to Day 1 and Day 2.

Finally, Fig. 13 displays the BESS power capacity, size, discharging energy, and charging energy between the baseline control and FAPC cases for Day 1, Day 2, and Day 3. Note that the BESS system is sized using the same method described in Section 4. In the first two test days (red and blue bars in Fig. 13), power capacity and discharging energy needs are very similar. The *power capacities* are both near 200 kW and *discharging energies* are near 400 kWh in the baseline control case. The third day is much lower however, near 100 kW and 80 kWh, respectively. On the other hand, the *BESS charging energy* and *BESS sizes* are very similar across all days in the baseline control scenario (near 500 kWh and 800 kWh, respectively). When analyzing Days 1 and 2 (red and blue bars), it can be seen that each category (power capacity, size, discharging energy, and charging energy) is reduced when using FAPC compared to the baseline case. Specifically, the BESS sizes are reduced by 80% and 79% in Days 1 and 2, respectively.

The orange bars in Fig. 13 show the BESS power capacity, size, discharging energy, and charging energy for Day 3 (weekend). While the difference in baseline control and FAPC profiles shown in Fig. 12 indicate that the load was indeed shifted, the total storage needs are similar for both the baseline and FAPC cases. This similarity can be seen by the smaller reduction in *BESS size* of 19.4%. As previously mentioned, this smaller improvement is most likely due to the reduction in the more flexible EV demand. Note that the size of the BESS is mostly determined by the amount of charging energy in Day 3. This means that the total demand is less than the RE generation; thus, an alternative to increasing the BESS size is to instead curtail the RE generation. This alternative would prove most significant in Day 3 but would apply to all scenarios.

Based solely on these results, the BESS should be sized by the Day 3 case, as it requires the largest BESS in terms of energy capacity. Admittedly, this 3-day sample size is not sufficient to accurately size the BESS for all possible cases. Future work involves examining more scenarios while scaling this system to include multiple buildings and charging stations each with different sizes and dynamics. With a larger, more realistic system, FAPC could be applied to more weather scenarios to get a better understanding for its robustness. A detailed and impactful cost savings analysis could then be conducted, eventually leading to real-world deployment of FAPC.

### 5.1. Individual subsystem performance

In this section, the individual subsystem performances using FAPC (Scenario 5) for each of the three test days in Table 2 are analyzed. Here, the objective is to show that even while the total demand is shifted considerably to track the RE generation signal, the performance of each individual subsystem is not sacrificed.

First, the performance of the building subsystem is analyzed. Fig. 14 shows that the internal temperature profile of the building remains within comfort bounds, but tends to fluctuate considerably throughout each simulation. In some instances, the temperature is in contact with a comfort bound, which is deemed unsatisfactory. Day 1 performs the best, where the temperature is in contact with $\underline{T}_b$ for only a short time near 16:40. This also occurs at a similar time in Day 2, but is in contact slightly longer. However, the performance of Day 3 is much worse. The temperature is in contact with $\underline{T}_b$ from nearly 11:00 to 17:00. Recall that in Day 3 (weekend), the EV demand is much lower. Therefore, the building consumes more energy in an attempt to track the RE generation. More power consumption in the building corresponds to a higher cooling load from the HVAC system, explaining why the temperature is near $\underline{T}_b$ in the afternoon.

Next, the performance of the EVCS subsystem is analyzed. The key objective for this subsystem is to ensure each EV is fully charged upon its departure time. Fig. 15 displays the $SoC$ of each EV throughout each simulation day. Note that at the beginning of the simulation each line starts at a different number between 0 and 1 (i.e., each EV has a different initial $SoC$). It can be seen from Fig. 15 that, each line (EV $SoC$)
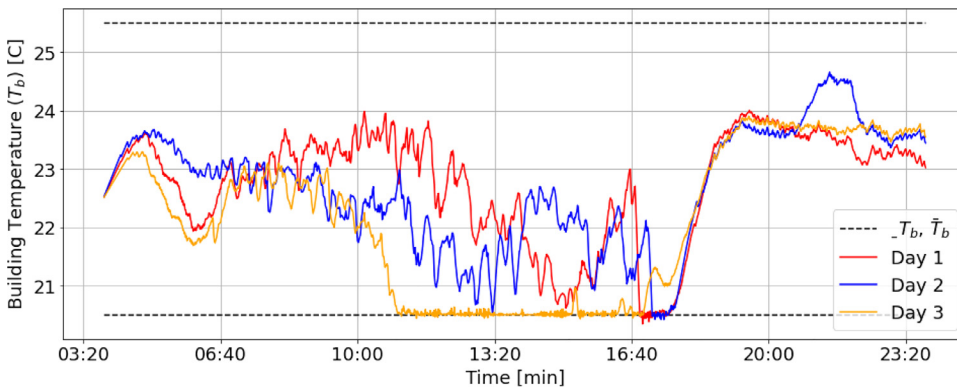
**Fig. 14.** Performance of the building subsystem under full control and coordination scenario (Scenario 5) for each simulation day (Table 2). The internal temperature profile is plotted for a perfect solar day (red) and bad solar day (blue) and a weekend (orange) to analyze its trajectory between comfort bounds (black dashed). (For interpretation of the references to colour in this figure legend, the reader is referred to the web version of this article.)
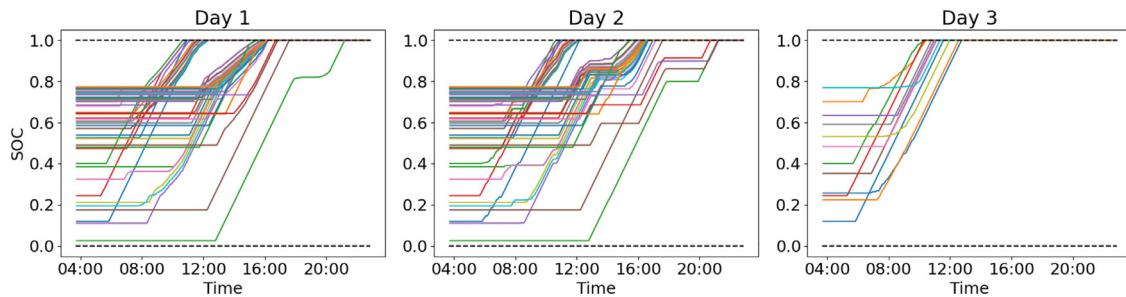


**Fig. 15.** Performance of the EVCS subsystem under full control and coordination scenario (Scenario 5 in Table 1) for each simulation day (Table 2). Each line in each plot represents the *SoC* of an EV in the EVCS. A value of 1 represents fully charged while 0 represents no charge.

**Table 3**

Types of forecasts used to analyze the forecast importance in FAPC.

| Forecast Scenario | 1 | 2 | 3 | 4 | 5 |
|---|---|---|---|---|---|
| Forecast Type | Perfect Forecast | Partial Forecast | Zero Forecast | Greedy Forecast | Random Forecast |

reaches a value of 1 by the end of the simulation. This implies that each EV is fully charged upon its departure time and the EVCS objective is effectively met in each test day. Note that there are considerably less lines in the weekend case and the slope of each line is fairly steep. This implies that that there are fewer EVs and their flexibility is quickly depleted, contributing to the lack in tracking performance in Day 3 as seen in Fig. 12.

### 5.2. Forecasting importance

The results in Sections 4 and 5 show how FAPC drastically improves tracking of the RE generation, even during days with inconsistent RE generation. The use of forecasts in FAPC is thought to be a major reason for this success. In this section, the importance of forecast accuracy is analyzed. Using Day 2 simulation data, FAPC is subjected to five different forecasts, as summarized in Table 3 and tracking performance of FAPC in each case is shown in Fig. 16.

The top plot in Fig. 16 shows the perfect forecast case. These results are identical to what is shown in the middle plot of Fig. 12. The orange line shows the EVDAP. The perfect forecast assumes perfect knowledge of 1) the EV charging events, 2) the building load, and 3) the RE generation. As can be seen from the orange line, the EVDAP matches the available power very well (offset due to building load).

The second plot shows the partial forecast case. The partial forecast is similar to the perfect forecast, only we assume that the building load and the RE generation signals are unknown. However, the EV

charging events are still perfectly known and used to create the EVDAP. Hence, the flat-top forecast shown by the orange line. With this EVDAP, the FAPC tracking shows a slightly lower demand than in the perfect forecast case. To quantify this difference, it is found that the necessary utility-scale BESS size is increased by 206% compared to the perfect forecast.

The middle plot shows the zero forecast case. As implied by the name, the EVDAP consists of all zeros (i.e., no load forecasted). Because the EV charging controller tracks the forecast, as expected, the EV charging load is reduced for the first two-thirds of the simulation. This reduction limits the EV charging early on, causing a spike in charging near the end of the day (near 16:40 and 20:00). This spike is a result of EVs nearing their departure times with insufficient states of charge. Hence, the controller must apply a higher charge rate to ensure full charge by their departure time. The required utility-scale BESS size is increased by 240% compared to the perfect forecast case.

The fourth plot shows the greedy forecast case. In this case, the EVDAP is the baseline control load profile. It can be seen that the EV load is increased early (near 08:00) and decreased later in the simulation in an attempt to track the EVDAP. Because of this, the necessary utility-scale BESS size is increased by 219% compared to the perfect forecast case.

The bottom plot shows the random forecast case. As implied by the name, this EVDAP is generated at random. While not too chaotic, this EVDAP obviously does not accurately forecast the available power to the EVs. Therefore, when the EV charging controller tracks this random EVDAP, an increase of 125% in utility-scale BESS size compared to the perfect forecast is observed.

The results presented in this section confirm that FAPC is indeed sensitive to the forecasts used to generate the EVDAP. Because perfect forecasts are used in this work, a sort of upper bound to the FAPC performance is established. Future work aims to investigate applying more realistic forecasts to account for weather uncertainties as well as stochastic building occupancy and EV events and will investigate how close to this upper bound the performance can be expected to be.
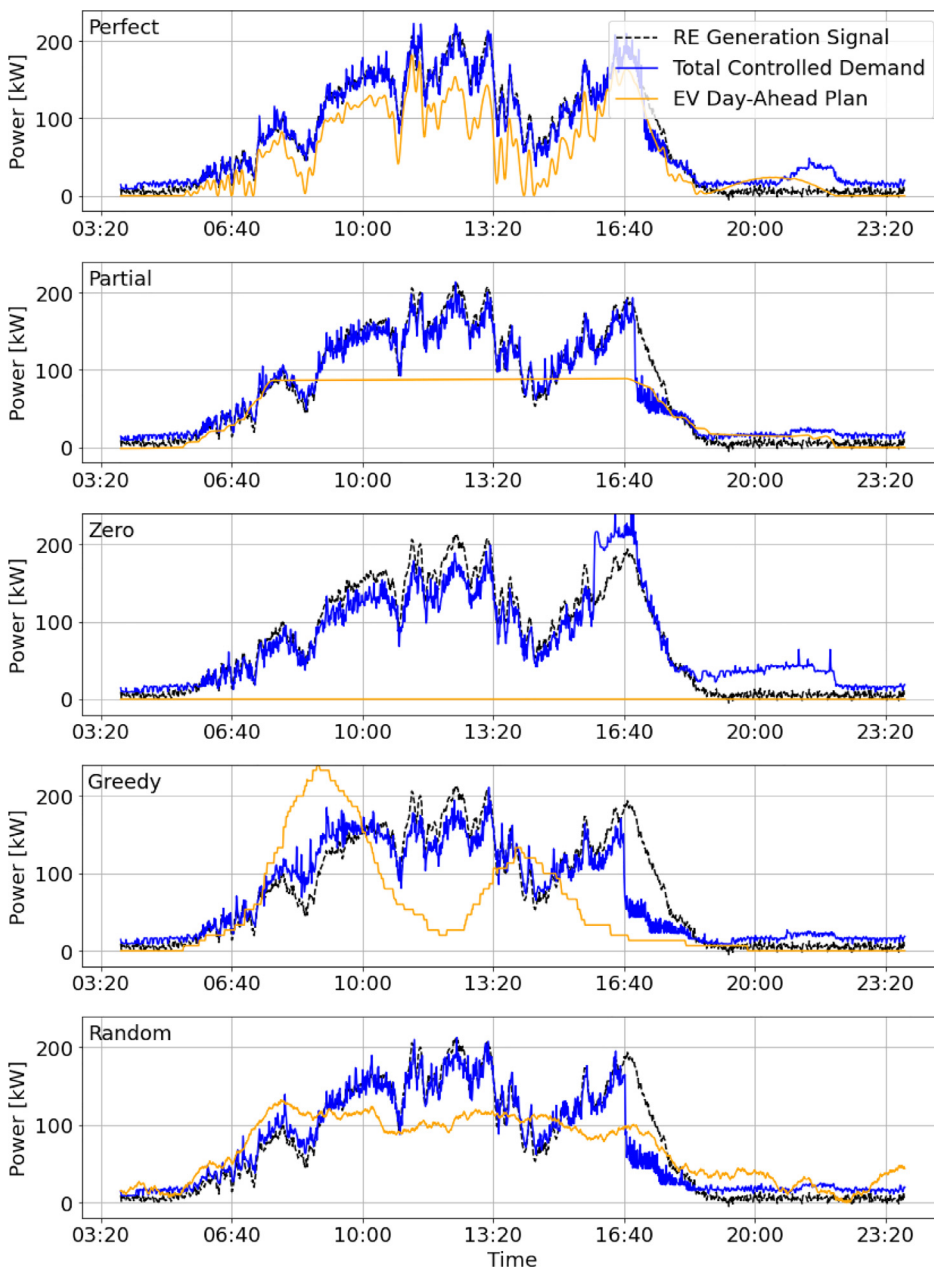
**Fig. 16.** Tracking performance of the FAPC algorithm when subjected to five different forecasts summarized in Table 3.

## 6. Conclusions

In this work, the novel forecast-aided predictive control (FAPC) algorithm is introduced. While leveraging the framework developed in works [42] and [43], FAPC introduces a new EV charging control algorithm. This algorithm utilizes forecasts to improve its real-time tracking ability. Instead of arbitrary reference signals, the performance of FAPC is evaluated using a realistic, RE generation scenario. The performance of FAPC is also evaluated across different weather and RE generation conditions and forecast accuracy. The performance of FAPC quantified by the size of the utility-level BESS required to enable perfect tracking in the system. This more realistic scenario corresponds to fully correlated disturbances, system loads, and system generation.

The results show that under FAPC, the demand can be shifted considerably to more closely track a RE generation signal. This significantly reduces the size of the required utility-scale BESS. A robustness analysis indicates that under days of more intermittent RE generation, FAPC continues to perform adequately. However, the performance of FAPC is decreased in a weekend case where demand is less significant and less

flexible. It is noted that despite a large amount of shifted demand, each subsystem still achieves its local objectives. Additionally, it was found that the FAPC tracking performance is indeed sensitive to the accuracy of the forecast.

## Declaration of Competing Interest

The authors declare that they have no known competing financial interests or personal relationships that could have appeared to influence the work reported in this paper.

## Data availability

Data will be made available on request.

## Acknowledgements

## Appendix

---

**Algorithm 1** Bisection algorithm.

---

**Ensure:** $P_{tol} = 0.001$
  **if** $P^{t,k} < P_{lb} + P_{tol}$ **then**
    $\mathbf{f}_{opt} \leftarrow \mathbf{f}_{lb}$
  **else if** $P^{t,k} > P_{up} - P_{tol}$ **then**
    $\mathbf{f}_{opt} \leftarrow \mathbf{f}_{ub}$
  **else**
    $\mathbf{f}_{opt} \leftarrow (\mathbf{f}_{lb} + \mathbf{f}_{ub})/2$
    **while** $(P_{ub} - P_{lb}) > P_{tol}$ **do**
      $\mathbf{f}_{opt} \leftarrow (\mathbf{f}_{lb} + \mathbf{f}_{ub})/2$
      $P_{curr} \leftarrow \sum_j^{\mathcal{J}} \left[ \frac{1}{\Delta_T}(SoC_j^d - SoC_j^a) - (T_j^d - t)(\bar{p}_j - \mathbf{f}) \right]_0^{\bar{p}_j}$
      **if** $P_{curr} < P^{t,k}$ **then**
        $\mathbf{f}_{lb} \leftarrow \mathbf{f}_{opt}$
        $\mathbf{P}_{lb} \leftarrow \mathbf{P}_{curr}$
      **else if** $P_{curr} > P^{t,k}$ **then**
        $\mathbf{f}_{ub} \leftarrow \mathbf{f}_{opt}$
        $\mathbf{P}_{ub} \leftarrow \mathbf{P}_{curr}$
      **end if**
    **end while**
  **end if**

---

---

**Algorithm 2** EVCS DA plan update.

---

  $MaxIter \leftarrow 10$
  **while** $iter < MaxIter$ **do**
    $P_{rt} \leftarrow f(P_{EV,DA})$ with $\omega_1, \omega_5 = 0$
    **for** $t \in \mathcal{T}$ **do**
      $P_{diff}^t \leftarrow (P_{EV,DA}^t + \delta^t) - P_{rt}^t$
      $\hat{\delta}^{1:t} \leftarrow \hat{\delta}^{t:t} + \frac{P_{diff}^t}{t}\mathbf{1}^T$
      $\hat{\delta}^{t+1:T} \leftarrow \hat{\delta}^{t+1:T} - \frac{P_{diff}^t}{T-t}\mathbf{1}^T$
      $\delta^t \leftarrow (1-\alpha)\delta^t + \alpha\hat{\delta}^t$
    **end for**
    $P_{EV,DA} \leftarrow P_{EV,DA} + \delta$
  **end while**

---

**Table 4**
Values of FAPC parameters used in producing results.

| Parameter | Value |
|---|---|
| $\eta$ | 17.5% (0.17) |
| $T_{ref}$ | 23.0 |
| $\underline{T}_b, \bar{T}_b$ | 20.5, 25.5 |
| $\underline{u}_1, \bar{u}_1$ | 0.0, 100.0 |
| $\underline{u}_2, \bar{u}_2$ | 10.0, 14.0 |
| $\underline{Q}_{HVAC}, \bar{Q}_{HVAC}$ | –600.0, 0.0 |
| $\Lambda$ | diag(0.001) |
| $Q$ | diag(5000,2,...,...) |
| $S$ | 0.0 |
| $[\omega_1, \omega_2, \omega_3, \omega_4, \omega_5]$ | [1.0, 1.0, 1.0, 1.0, 0.9] |

## References

[1] Renewables became the second-most prevalent U.S. electricity source in 2020. https://www.eia.gov/todayinenergy/detail.php?id=48896.

[2] Kumar GVB, Sarojini RK, Palanisamy K, Padmanaban S, Holm-Nielsen JB, et al. Large scale renewable energy integration: issues and solutions. Energies 2019;12(10):1996. doi:10.3390/en12101996. Number: 10 Publisher: Multidisciplinary Digital Publishing Institute

[3] Quadrennial Technology Review 2015. https://www.energy.gov/quadrennial-technology-review-2015.

[4] Grid Integration Toolkit. https://greeningthegrid.org/Grid-Integration-Toolkit/gridintegration-homepage.

[5] Dwyer M.. Electric vehicles and hybrids surpass 10% of U.S. light-duty vehicle sales. https://www.eia.gov/todayinenergy/detail.php?id=51218.

[6] McKerracher C, Izadi-Najafabadi A, O'Donovan A, Albanese N, Souloopolous N, Doherty D, Boers M, Fisher R, Cantor C, Frith J, Mi S, Grant A. Electric vehicle outlook 2020. Tech. Rep.. BloombergNEF; 2020.

[7] Zummo P.. Electrifying the Future: Current Trends, Future Pathways, and Potential Challenges | American Public Power Association. 2022. https://www.publicpower.org/resource/electrifying-future-current-trends-future-pathways-and-potential-challenges.

[8] U. E. I. A. (EIA). U.S. energy facts explained - consumption and production - U.S. Energy Information Administration (EIA). 2022. https://www.eia.gov/energyexplained/us-energy-facts/.

[9] Dayem K, Mercier C, May-Ostendorp P. Electric vehicle charging control strategies. Tech. Rep.. National Rural Electric Cooperative Association's Business and Technology Strategies department; 2019.

[10] Ma Z, Callaway DS, Hiskens IA. Decentralized charging control of large populations of plug-in electric vehicles. IEEE Trans Control Syst Technol 2013;21(1):67–78. doi:10.1109/TCST.2011.2174059.

[11] Liu M, Phanivong PK, Shi Y, Callaway DS. Decentralized charging control of electric vehicles in residential distribution networks. IEEE Trans Control Syst Technol 2019;27(1):266–81. doi:10.1109/TCST.2017.2771307.

[12] Wu D, Radhakrishnan N, Huang S. A hierarchical charging control of plug-in electric vehicles with simple flexibility model. Appl Energy 2019;253:113490.

[13] Di Giorgio A, Liberati F, Canale S. Electric vehicles charging control in a smart grid: amodel predictive control approach. Control Eng Pract 2014;22:147–62.

[14] López MA, De La Torre S, Martín S, Aguado JA. Demand-side management in smart grid operation considering electric vehicles load shifting and vehicle-to-grid support. International Journal of Electrical Power & Energy Systems 2015;64:689–98.

[15] Tuchnitz F, Ebell N, Schlund J, Pruckner M. Development and evaluation of a smart charging strategy for an electric vehicle fleet based on reinforcement learning. Appl Energy 2021;285:116382. doi:10.1016/j.apenergy.2020.116382. https://www.sciencedirect.com/science/article/pii/S0306261920317566

[16] Majidpour M, Qiu C, Chu P, Pota HR, Gadh R. Forecasting the EV charging load based on customer profile or station measurement? Appl Energy 2016;163:134–41. doi:10.1016/j.apenergy.2015.10.184. https://www.sciencedirect.com/science/article/pii/S0306261915014348

[17] Huber J, Dann D, Weinhardt C. Probabilistic forecasts of time and energy flexibility in battery electric vehicle charging. Appl Energy 2020;262:114525. doi:10.1016/j.apenergy.2020.114525. https://www.sciencedirect.com/science/article/pii/S0306261920300374

[18] Xydas ES, Marmaras CE, Cipcigan LM, Hassan AS, Jenkins N. Forecasting electric vehicle charging demand using support vector machines. In: 2013 48th International Universities' Power Engineering Conference (UPEC); 2013. p. 1–6. doi:10.1109/UPEC.2013.6714942.

[19] Kodaira D, Kondoh J. Probabilistic forecasting model for non-normally distributed EV charging demand. In: 2020 International Conference on Smart Grids and Energy Systems (SGES); 2020. p. 623–6. doi:10.1109/SGES51519.2020.00116.

[20] Islam MS, Mithulananthan N, Hung DQ. A day-ahead forecasting model for probabilistic EV charging loads at business premises. IEEE Trans Sustainable Energy 2018;9(2):741–53. doi:10.1109/TSTE.2017.2759781.

[21] Van Kriekinge G, De Cauwer C, Sapountzoglou N, Coosemans T, Messagie M. Day-ahead forecast of electric vehicle charging demand with deep neural networks. World Electric Vehicle Journal 2021;12(4). doi:10.3390/wevj12040178.

[22] Bessa RJ, Matos MA. Global against divided optimization for the participation of an EV aggregator in the day-ahead electricity market. part II: numerical analysis. Electr Power Syst Res 2013;95:319–29. doi:10.1016/j.epsr.2012.08.013. https://www.sciencedirect.com/science/article/pii/S0378779612002660

[23] Drgoňa J, Kvasnica M. Comparison of MPC strategies for building control. In: 2013 International Conference on Process Control (PC); 2013. p. 401–6. doi:10.1109/PC.2013.6581444.

[24] Martinčević A, Vašak M, Lešić V. Model predictive control for energy-saving and comfortable temperature control in buildings. In: 2016 24th Mediterranean Conference on Control and Automation (MED); 2016. p. 298–303. doi:10.1109/MED.2016.7536001.

[25] Oldewurtel F, Ulbig A, Parisio A, Andersson G, Morari M. Reducing peak electricity demand in building climate control using real-time pricing and model predictive control. In: 49th IEEE Conference on Decision and Control (CDC); 2010. p. 1927–32. doi:10.1109/CDC.2010.5717458.

[26] Oldewurtel F, Parisio A, Jones CN, Gyalistras D, Gwerder M, Stauch V, et al. Use of model predictive control and weather forecasts for energy efficient building climate control. Energy Build 2012;45:15–27. doi:10.1016/j.enbuild.2011.09.022. https://www.sciencedirect.com/science/article/pii/S0378778811004105

[27] Camponogara E, Jia D, Krogh BH, Talukdar S. Distributed model predictive control. IEEE Control Syst Mag 2002;22(1):44–52. doi:10.1109/37.980246.

[28] Eini R, Abdelwahed S. Distributed model predictive control based on goal coordination for multi-zone building temperature control. In: 2019 IEEE Green Technologies Conference (GreenTech); 2019. p. 1–6. doi:10.1109/GreenTech.2019.8767123.

[29] Bay CJ, Chintala R, Rasmussen BP. Steady-state predictive optimal control of integrated building energy systems using a mixed economic and occupant comfort focused objective function. Energies 2020;13(11):2922.

[30] Yang S, Wan MP, Chen W, Ng BF, Dubey S. Model predictive control with adaptive machine-learning-based model for building energy efficiency and comfort optimization. Appl Energy 2020;271:115147.

[31] Drgoňa J, Tuor AR, Chandan V, Vrabie DL. Physics-constrained deep learning of multi-zone building thermal dynamics. Energy Build 2021;243:110992. doi:10.1016/j.enbuild.2021.110992. https://www.sciencedirect.com/science/article/pii/S0378778821002760

[32] Contreras-OcaŞa JE, Sarker MR, Ortega-Vazquez MA. Decentralized coordination of a building manager and an electric vehicle aggregator. IEEE Trans Smart Grid 2018;9(4):2625–37. doi:10.1109/TSG.2016.2614768.

[33] Costanzo GT, Gehrke O, Bondy DEM, Sossan F, Bindner H, Parvizi J, Madsen H. A coordination scheme for distributed model predictive control: Integration of flexible DERs. In: IEEE PES ISGT Europe 2013; 2013. p. 1–5. doi:10.1109/ISGTEurope.2013.6695474.

[34] Quddus MA, Shahvari O, Marufuzzaman M, Usher JM, Jaradat R. A collaborative energy sharing optimization model among electric vehicle charging stations, commercial buildings, and power grid. Appl Energy 2018;229:841–57.

[35] Huang P, Lovati M, Zhang X, Bales C. A coordinated control to improve performance for a building cluster with energy storage, electric vehicles, and energy sharing considered. Appl Energy 2020;268:114983.

[36] Yang Y, Jia Q-S, Deconinck G, Guan X, Qiu Z, Hu Z. Distributed coordination of EV charging with renewable energy in a microgrid of buildings. IEEE Trans Smart Grid 2018;9(6):6253–64. doi:10.1109/TSG.2017.2707103.

[37] Thomas D, Deblecker O, Ioakimidis CS. Optimal operation of an energy management system for a grid-connected smart building considering photovoltaics uncertainty and stochastic electric vehicles driving schedule. Appl Energy 2018;210:1188–206. doi:10.1016/j.apenergy.2017.07.035. https://www.sciencedirect.com/science/article/pii/S0306261917309078

[38] liu z, Wu Q, Shahidehpour M, Li C, Huang S, Wei W. Transactive real-time electric vehicle charging management for commercial buildings with PV on-site generation. IEEE Trans Smart Grid 2019;10(5):4939–50. doi:10.1109/TSG.2018.2871171.

[39] Yoon S, Hwang E. Load guided signal-based two-stage charging coordination of plug-in electric vehicles for smart buildings. IEEE Access 2019;7:144548–60. doi:10.1109/ACCESS.2019.2945483.

[40] Yoon S, Hwang E. Price control-based decentralized electric vehicle charging coordination by arbitration type aggregators for smart buildings. In: 2021 IEEE International Smart Cities Conference (ISC2); 2021. p. 1–4. doi:10.1109/ISC253183.2021.9562835.

[41] Iria J, Soares F, Matos M. Optimal bidding strategy for an aggregator of prosumers in energy and secondary reserve markets. Appl Energy 2019;238:1361–72. doi:10.1016/j.apenergy.2019.01.191. https://www.sciencedirect.com/science/article/pii/S0306261919301928

[42] Wald D, King J, Bay CJ, Chintala R, Johnson K. Integration of distributed controllers: power reference tracking through charging station and building coordination. Appl Energy 2022;314:118753. doi:10.1016/j.apenergy.2022.118753. https://www.sciencedirect.com/science/article/pii/S0306261922002070

[43] Wald D, Johnson K, Bay CJ, King J, Chintala R. Grid-interactive electric vehicle and building coordination using coupled distributed control. Tech. Rep.. National Renewable Energy Lab(NREL), Golden, CO (United States); 2022.

[44] Jalal RE, Rasmussen BP. Limited-communication distributed model predictive control for coupled and constrained subsystems. IEEE Trans on Control Systems Technology 2017;25(5):1807–15. doi:10.1109/TCST.2016.2615088.

[45] Bay CJ, Chintala R, Chinde V, King J. Distributed model predictive control for coordinated, grid-interactive buildings. Appl Energy 2022;312:118612. doi:10.1016/j.apenergy.2022.118612. https://www.sciencedirect.com/science/article/pii/S0306261922000861

[46] Comden J, Yao S, Chen N, Xing H, Liu Z. Online optimization in cloud resource provisioning: predictions, regrets, and algorithms. Proc ACM Meas Anal Comput Syst 2019;3(1). doi:10.1145/3322205.3311087.

[47] Xu Z, Su W, Hu Z, Song Y, Zhang H. A hierarchical framework for coordinated charging of plug-in electric vehicles in china. IEEE Trans Smart Grid 2016;7(1):428–38. doi:10.1109/TSG.2014.2387436.

[48] Wood E.W., Rames C.L., Muratori M.. New EVSE analytical tools/models: Electric vehicle infrastructure projection tool (EVI-pro) 2018; https://www.osti.gov/biblio/1419413.

[49] NSRDB. https://nsrdb.nrel.gov/.

[50] NREL. Floris. version 2.4. 2021. https://github.com/NREL/floris.